

## Light cone effect on the reionization 21-cm signal – II. Evolution, anisotropies and observational implications

Article (Published Version)

Datta, Kanan K, Jensen, Hannes, Majumdar, Suman, Mellema, Garrelt, Iliev, Ilian T, Mao, Yi, Shapiro, Paul R and Ahn, Kyungjin (2014) Light cone effect on the reionization 21-cm signal – II. Evolution, anisotropies and observational implications. *Monthly Notices Of The Royal Astronomical Society*, 442 (2). pp. 1491-1506. ISSN 0035-8711

This version is available from Sussex Research Online: <http://sro.sussex.ac.uk/id/eprint/69074/>

This document is made available in accordance with publisher policies and may differ from the published version or from the version of record. If you wish to cite this item you are advised to consult the publisher's version. Please see the URL above for details on accessing the published version.

### **Copyright and reuse:**

Sussex Research Online is a digital repository of the research output of the University.

Copyright and all moral rights to the version of the paper presented here belong to the individual author(s) and/or other copyright owners. To the extent reasonable and practicable, the material made available in SRO has been checked for eligibility before being made available.

Copies of full text items generally can be reproduced, displayed or performed and given to third parties in any format or medium for personal research or study, educational, or not-for-profit purposes without prior permission or charge, provided that the authors, title and full bibliographic details are credited, a hyperlink and/or URL is given for the original metadata page and the content is not changed in any way.

# Light cone effect on the reionization 21-cm signal – II. Evolution, anisotropies and observational implications

Kanan K. Datta,<sup>1,2★</sup> Hannes Jensen,<sup>2</sup> Suman Majumdar,<sup>2</sup> Garrelt Mellema,<sup>2</sup>  
Ilian T. Iliev,<sup>3</sup> Yi Mao,<sup>4</sup> Paul R. Shapiro<sup>5</sup> and Kyungjin Ahn<sup>6</sup>

<sup>1</sup>National Centre For Radio Astrophysics, Post Bag 3, Ganeshkhind, Pune 411 007, India

<sup>2</sup>Department of Astronomy and Oskar Klein Centre, AlbaNova, Stockholm University, SE-106 91 Stockholm, Sweden

<sup>3</sup>Astronomy Centre, Department of Physics and Astronomy, Pevensey II Building, University of Sussex, Falmer, Brighton BN1 9QH, UK

<sup>4</sup>Institut Lagrange de Paris, Institut d'Astrophysique de Paris, CNRS, UPMC Université Paris 06, UMR7095, 98 bis, boulevard Arago, F-75014 Paris, France

<sup>5</sup>Department of Astronomy and Texas Cosmology Center, University of Texas, Austin, TX 78712, USA

<sup>6</sup>Department of Earth Sciences, Chosun University, Gwangju 501-759, Korea

Accepted 2014 May 6. Received 2014 May 6; in original form 2014 February 6

## ABSTRACT

Measurements of the H I 21-cm power spectra from the reionization epoch will be influenced by the evolution of the signal along the line-of-sight direction of any observed volume. We use numerical as well as seminumerical simulations of reionization in a cubic volume of 607 Mpc across to study this so-called light-cone effect on the H I 21-cm power spectrum. We find that the light-cone effect has the largest impact at two different stages of reionization: one when reionization is  $\sim 20$  per cent and other when it is  $\sim 80$  per cent completed. We find a factor of  $\sim 4$  amplification of the power spectrum at the largest scale available in our simulations. We do not find any significant anisotropy in the 21-cm power spectrum due to the light-cone effect. We argue that for the power spectrum to become anisotropic, the light-cone effect would have to make the ionized bubbles significantly elongated or compressed along the line of sight, which would require extreme reionization scenarios. We also calculate the two-point correlation functions parallel and perpendicular to the line of sight and find them to differ. Finally, we calculate an optimum frequency bandwidth below which the light-cone effect can be neglected when extracting power spectra from observations. We find that if one is willing to accept a 10 per cent error due to the light-cone effect, the optimum frequency bandwidth for  $k = 0.056 \text{ Mpc}^{-1}$  is  $\sim 7.5$  MHz. For  $k = 0.15$  and  $0.41 \text{ Mpc}^{-1}$ , the optimum bandwidth is  $\sim 11$  and  $\sim 16$  MHz, respectively.

**Key words:** methods: numerical – methods: statistical – cosmology: theory – dark ages, reionization, first stars – diffuse radiation.

## 1 INTRODUCTION

A period of major changes in the Universe took place between  $\sim 0.3$  and  $\sim 1$  billion years after the big bang at the time when the first galaxies and supermassive black holes were forming. These first structures produced ionizing radiation which escaped from the parent environment to spread through the intergalactic medium (IGM) and ionize the neutral hydrogen (H I) in it. This period is known as the Epoch of Reionization (EoR). Our knowledge about this epoch in the evolution of the Universe is currently very limited as even the most powerful telescopes can only offer a glimpse of objects from this time. Observations of the redshifted 21-cm signal from H I in

the IGM are expected to unveil how the reionization process progressed and will thus provide us with invaluable information about this epoch (see e.g. Pritchard & Loeb 2012; Mellema et al. 2013, for reviews).

A great deal of effort during recent years, both in theory and in observations, has put ‘reionization with 21-cm radiation’ at the forefront of the modern astronomy (Morales & Wyithe 2010). The first generation of low-frequency radio telescopes such as Low Frequency Array<sup>1</sup> (van Haarlem et al. 2013), Giant Metrewave Radio Telescope<sup>2</sup> (Pen et al. 2008), Murchison Widefield Array<sup>3</sup> (Tingay

★E-mail: [kanan@ncra.tifr.res.in](mailto:kanan@ncra.tifr.res.in)

<sup>1</sup> <http://www.astro.rug.nl/eor>

<sup>2</sup> <http://gmrt.ncra.tifr.res.in/>

<sup>3</sup> <http://www.mwatelescope.org>

et al. 2013), Precision Array for Probing the EoR<sup>4</sup> (Parsons et al. 2010) have started providing us with results such as preliminary measurements of the foregrounds at EoR frequencies (Ali, Bharadwaj & Chengalur 2008; Bernardi et al. 2009; Pen et al. 2009; Ghosh et al. 2012; Bernardi et al. 2013; Jacobs et al. 2013; Yatawatta et al. 2013) as well as limits on reionization (Bowman & Rogers 2010; Paciga et al. 2013; Parsons et al. 2013).

These telescopes may be able to detect large individual ionized regions embedded in H I (Datta, Bharadwaj & Choudhury 2007; Geil & Wyithe 2008; Datta et al. 2012a; Majumdar, Bharadwaj & Choudhury 2012; Malloy & Lidz 2013) or provide crude maps of large H I regions (Zaroubi et al. 2012; Chapman et al. 2013). However, they will primarily try to detect the EoR H I 21-cm signal statistically, using quantities such as the power spectrum (Morales & Hewitt 2004; Zaldarriaga, Furlanetto & Hernquist 2004; Harker et al. 2010), visibility correlations (Bharadwaj & Ali 2005; Ali et al. 2008), variance (Mellema et al. 2006b; Jelić et al. 2008; Bittner & Loeb 2011; Patil et al. 2014) and skewness (Harker et al. 2009) of the H I 21-cm brightness temperature fluctuations. Understanding these statistical quantities and their connection to the physics of reionization is crucial in planning the observational strategies, analysing and validating the observations and extracting the reionization characteristics from them. Substantial efforts on the theoretical side have been undertaken towards this. For example, analytic models of reionization which are very fast but less accurate have been developed (Furlanetto, Zaldarriaga & Hernquist 2004). Despite many challenges, there has been significant progress in estimating the large-scale H I 21-cm signal from the entire EoR through numerical (Iliev et al. 2006; Mellema et al. 2006b; Maselli et al. 2007; McQuinn et al. 2007; Shin, Trac & Cen 2008; Baek et al. 2009) and seminumerical simulations (Mesinger & Furlanetto 2007; Zahn et al. 2007; Geil & Wyithe 2008; Santos et al. 2008; Choudhury, Haehnelt & Regan 2009; Thomas et al. 2009; Battaglia et al. 2013).

Numerical simulations of the EoR which calculate the ionization state of the IGM by solving the proper radiative transfer equation at each cell in the simulation box can be highly accurate. Such simulations can conserve the total photon numbers emitted by all sources, introduce complex photon production histories for the sources and can take into account the effect of recombination self-consistently. However, they do require substantial computational resources in order to achieve this (Iliev et al. 2014). On the other hand, seminumerical simulations, which simply compare the total number of ionizing photons available and the number of baryons to be ionized in order to calculate the ionization state, require much less resources. Although approximate in nature, recent studies show that at least for simplified source models, seminumerical simulations can produce reasonable results with up to  $\sim 10$  per cent error in the power spectrum estimates (see e.g. Majumdar et al. 2014, for a recent study). The availability of numerical and seminumerical simulations allow us to explore various source models and study important issues such as the light-cone (LC) effect, redshift space distortions, sinks, very bright QSOs, different feedback mechanisms, etc., on the observable statistical quantities mentioned above. The simulated signal can also be used to determine the detectability of various observables, explore different foreground subtraction methods and test for other systematics.

In this paper, we study in detail the impact of the so-called LC effect on the EoR H I 21-cm signal. Since the signal originates

from a line transition, different cosmological epochs correspond to different wavelengths, characterized by their cosmological redshift  $z$  through

$$\lambda_{\text{obs}} = \lambda_{\text{emitted}}(1 + z). \quad (1)$$

This means that an observational data set containing a range of wavelengths corresponds to a time period in which the signal may have evolved. This is commonly known as the LC effect. The radio telescope data will be in the form of three-dimensional image cubes of images over a wide range of frequencies. The analysis of these 3D data sets should generally take into account this LC effect.

In Datta et al. (2012b) (hereafter [Paper I](#)), we presented the first numerical investigation of the LC effect on the spherically averaged H I 21-cm power spectrum. We used the results of large volume numerical simulations [163 Mpc (comoving) on each side] and studied the effect at four different stages of reionization. We found that the effect mostly ‘averages out’, but can lead to a change of  $\sim 50$  per cent in the power spectrum at scales around  $k \sim 0.1 \text{ Mpc}^{-1}$ . We also attempted to study the LC anisotropy in the signal but the simulation volume was too small to quantify this properly. In the analysis, we also incorporated redshift space distortions (due to the gas peculiar velocity) and found them to have a negligible impact on the LC effect (see Section 5 and fig. 14 in [Paper I](#)).

La Plante et al. (2013) used a larger volume<sup>5</sup> and focused on similar issues. They reported significant anisotropies in the full signal but also noted that radio interferometric experiments, which only measure fluctuations in the signal and therefore exclude certain Fourier modes, will observe the signal to be isotropic.

Another way to characterize the LC effect is to compare the two-point correlation function of the signal along and perpendicular to the line of sight. Barkana & Loeb (2006) adopted this approach in the first, analytic study of LC anisotropies in the 21-cm signal. Zawada et al. (2014) followed the same approach, using the results of large-scale reionization simulations of size  $\approx 571 \text{ Mpc}$ . They extended their investigations to the pre-reionization epochs where the spin temperature of H I is lower or comparable to the cosmic microwave background (CMB) temperature and the signal may appear in absorption against the CMB. Both these works report anisotropies due to the LC effect although the properties of these anisotropies differ between them.

In this paper, we use the largest radiative transfer simulation of the EoR to date to study the LC effect further and on larger scales than we did in [Paper I](#). Although the radiative transfer simulation is more accurate, the associated computational costs make it difficult to explore a range of parameters. To explore the LC effect for other possible reionization models and study the robustness of some of our findings, we use a seminumerical reionization simulation of the same volume. Additionally, we employ some toy models to understand our findings. We focus on the following issues.

(i) Evolution of the LC effect. At what stages and scales of reionization is the effect important? How do redshift space distortions and the LC effect interact?

(ii) Anisotropy in the 21-cm power spectrum. Does the LC effect introduce any anisotropy?

(iii) Two-point correlation analysis of the 21-cm signal. How does the LC effect show up and does it introduce anisotropy?

(iv) Impact on analysis strategy. What frequency bandwidths can be used to minimize the LC effect?

<sup>4</sup> <http://eor.berkeley.edu/>

<sup>5</sup> The size of the full box is  $2/h \text{ Gpc}$ , but they use sub-volumes of line-of-sight extent up to  $500 \text{ Mpc}$  for the LC analysis.

The outline of the paper is as follows. Section 2 briefly describes our reionization simulations, numerical and seminumerical, and how we produce mock 21-cm data cubes including the LC effect and redshift space distortions. We introduce the H I 21-cm power spectrum and its anisotropies in Section 3. We present our results on the impact of the LC effect on the 21-cm power spectrum, both the spherically averaged version and the anisotropy, in Section 4. Section 5 presents the results of simple analytic and toy models which help in understanding our LC anisotropy results and provide insight into which conditions introduce LC anisotropies in the power spectrum. Results on the two-point correlation function are described in Section 6. Section 7 discusses the impact of the LC effect on the power spectrum derived from observations. Here, we also provide an optimal frequency bandwidth below which the complications due to the LC effect are mostly avoided. Finally, we summarize the results and conclude in Section 8.

We assume a flat  $\Lambda$ CDM model with parameters  $\Omega_m = 0.27$ ,  $\Omega_b = 0.044$ ,  $h = 0.7$ ,  $n = 0.96$ ,  $\sigma_8 = 0.8$ , consistent with the nine-year *Wilkinson Microwave Anisotropy Probe* (WMAP) results (Hinshaw et al. 2013) and *Planck* (Planck Collaboration et al. 2013).

## 2 SIMULATING THE REIONIZATION 21-CM SIGNAL

### 2.1 *N*-body and radiative transfer simulations

The basis of our reionization simulations is an  $(607 \text{ Mpc})^3$  *N*-body simulation performed with the CUBEP<sup>3</sup>M code and post-processed with the C<sup>2</sup>-RAY code (see Iliev et al. 2014 for details). CUBEP<sup>3</sup>M (Harnois-Déraps et al. 2013) is a cosmological *N*-body code based on PMFAST (Merz, Pen & Trac 2005). It calculates gravitational forces on a particle–particle basis for short distances and using a grid for long distances. Here, we used 5488<sup>3</sup> particles, each with a mass of  $5 \times 10^7 M_\odot$ , and a grid with 10 976<sup>3</sup> cells which gives a spatial resolution of  $\sim 5.5$  kpc. We note that in a P<sup>3</sup>M *N*-body code, the resolution is determined by the gravitational force softening instead of the cell size. Outputs from this simulation have been recorded at intervals of 11.5 Myr in the redshift range  $z = 6$ –30. This yields a total 76 simulation boxes of dark matter distribution. For each CUBEP<sup>3</sup>M output, we use a halo finder to locate dark matter haloes and measure their masses. The halo finder is based on the spherical overdensity method and a group of more than 20 particles with overdensity  $\Delta > 178$  with respect to the mean dark matter density is considered to be halo. This provides us with a list of dark matter haloes with masses down to  $\sim 10^9 M_\odot$  together with their positions.

It is believed that dark matter haloes with masses as low as  $\sim 10^8 M_\odot$  would be able to form stars through atomic cooling and thus contribute to reionization. To resolve such low-mass haloes, we would need to use 10 times more particles compared to what we use here, which is computationally unfeasible. Instead, we use a sub-grid recipe calibrated through a higher mass resolution but smaller volume simulation [volume  $(163 \text{ Mpc})^3$ , 3072<sup>3</sup> particles] to introduce haloes down to  $10^8 M_\odot$ . The results of this simulation give us the total mass in haloes of masses between  $10^8$  and  $10^9 M_\odot$  as a function of redshift and density in volumes of size 1.2 Mpc, this being the size of cells in our radiative transfer grid. Our method reproduces the mean dark matter halo mass function for the entire box but it neglects the scatter in the local overdensity–halo number relation which is observed numerically. We then combine the local total mass for the missing haloes with the dark matter halo list

obtained directly by the halo finder method to create a full list of ionizing sources.

Using the halo lists and density field outputs – down-sampled to 504<sup>3</sup> cells or a resolution of 1.2 Mpc – we then simulated the reionization of the IGM using C<sup>2</sup>-RAY (Mellema et al. 2006a). C<sup>2</sup>-RAY works by casting rays from ionizing sources and iteratively solving for the evolution of the ionized fraction of hydrogen in each point on the grid. The dark matter haloes from the *N*-body simulations were used as ionizing sources, which each halo with mass  $M_h$  assumed to have an ionizing flux:

$$\dot{N}_\gamma = g_\gamma \frac{M_h \Omega_b}{(10 \text{ Myr}) \Omega_m m_p}, \quad (2)$$

where  $m_p$  is the proton mass and  $g_\gamma$  is a source efficiency coefficient, effectively incorporating the star formation efficiency, the initial mass function and the fraction of ionizing photons escaping into the IGM. Here, we use

$$g_\gamma = \begin{cases} 1.7 & \text{for } M_h \geq 10^9 M_\odot \\ 7.1 & \text{for } M_h < 10^9 M_\odot, \end{cases} \quad (3)$$

motivated by the fact that low-mass haloes should have a higher escape fraction and more top-heavy initial mass function. These low-mass haloes are turned off completely when the local ionized fraction exceeds 10 per cent since they lack the gravitational well to keep accreting material in a highly ionized environment (Iliev et al. 2007).

### 2.2 Light-cone volumes

From the steps described above, we obtain a series of simulation volumes of the dark matter distribution and the ionization state of the IGM, each at a constant redshift (‘coeval’ cubes). We then calculate the H I 21-cm brightness temperature,  $\delta T_b(\mathbf{r}, z)$ , in these volumes as

$$\delta T_b(\mathbf{r}, z) = \widehat{\delta T}_b(z) [1 + \delta_{\text{HI}}(\mathbf{r})], \quad (4)$$

where  $\widehat{\delta T}_b(z)$  is the global mean 21-cm brightness temperature at redshift  $z$  and  $\delta_{\text{HI}}(\mathbf{r})$  is the overdensity of neutral gas in some point  $\mathbf{r}$ . This equation is only valid once the spin temperature of the IGM is much higher than the CMB temperature, which should be true in all but the earliest stages of reionization.

Next, we need to transform these into LC volumes, i.e. volumes where the evolution state of the IGM changes along the line of sight. We do this by stepping through redshifts and for each redshift  $z$ , find two coeval cubes whose redshifts bracket  $z$  and interpolate between these two cubes. The exact procedure is described in detail in Paper I.

After this step, we end up with a volume consisting of cells of constant comoving size, but where the evolutionary state of the IGM along the line of sight matches what an observer would actually see. A slice through the H I 21-cm brightness temperature from the LC volume is shown in Fig. 1. Note that, although our LC volume extends to around 1821 Mpc along the line-of-sight axis, we only use at most 607 Mpc for our analysis. Since the size of our individual simulation cubes are  $(607 \text{ Mpc})^3$ , any statistics for larger distances will be affected by periodicity effects.

### 2.3 Redshift space distortions

We also wish to study the LC effect together with the redshift space distortions introduced by gas peculiar velocities. Since the redshift of a parcel of gas is determined not only by its cosmological redshift



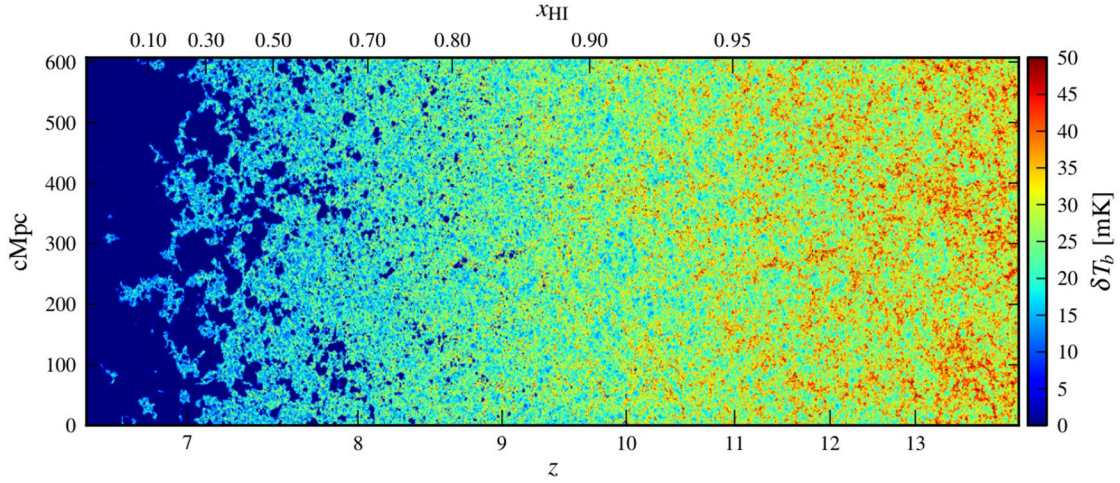


**Figure 1.** A slice through the 21-cm brightness temperature LC volume from the numerical simulation.

but also by the line-of-sight component of its peculiar velocity, the signal that one would reconstruct by translating redshifts to line-of-sight positions is not the same as the real-space signal. Matter tends to flow towards high-density regions, and away from low-density voids, which causes the 21-cm signal in redshift space to become anisotropic. The signal also has a higher contrast than in real space. See Bharadwaj & Ali (2005) and Mao et al. (2012) for detailed reviews of the theory of redshift space distortions.

We incorporate this effect using the MM-RRM scheme described in detail in Mao et al. (2012). In short, this method works by moving the boundaries of each cell according to the gas velocity at the position at the boundary. A cell boundary at a real-space position  $\mathbf{r}$  is moved to a redshift space position  $\mathbf{s}$ :

$$\mathbf{s} = \mathbf{r} + \frac{1 + z_{\text{obs}}}{H(z_{\text{obs}})} v_{\parallel}(\mathbf{r}, \mathbf{r}) \hat{\mathbf{r}}, \quad (5)$$

where  $z_{\text{obs}}$  is the observed redshift of the cell and  $v_{\parallel}$  is the line-of-sight component of the gas peculiar velocity at this position. Typically, gas velocities are of the order of a few hundred  $\text{km s}^{-1}$ , resulting in cell boundary displacements that can reach up to 2 or even 3 cMpc in the most dense regions. Since we interpolate the velocity over the cell, any velocity gradient across the cell will cause the cell to be stretched or compressed in redshift space and the 21-cm signal to either decrease or increase, respectively. After this step, we re-grid the redshift space data to the original cell size. This entire procedure is carried out after constructing the LC data volumes, since applying the effects in the other order would lead to unphysical results at the edges of the coeval data volumes.

## 2.4 Seminumerical simulations

We have just one realization of reionization based on the radiative transfer simulation described earlier in this section. However, there is a considerable uncertainty in the nature and luminosity of the sources of reionization. For example, reionization may be considerably earlier and faster than in our numerical simulation. It is anticipated that such a rapid reionization may enhance the LC anisotropy in the signal (Barkana & Loeb 2006). However, it is computationally expensive to rerun our radiative transfer simulation to generate many different scenarios. We side step this issue by using a seminumerical method to simulate such an early and rapid reionization and test whether that enhances the LC anisotropy in the observables of the 21-cm signal.

This seminumerical simulation employs the method described in Choudhury et al. (2009). This method is inspired by the excursion-set formalism (Furlanetto et al. 2004) and closely follows the methodology described in Mesinger & Furlanetto (2007), with some differences. Like all other reionization models, here we also assume that the ionizing photons were produced in dark matter haloes. Due to the lack of knowledge about the properties of the sources of these photons, we assume that the total number of ionizing photons produced in a halo of mass  $M_h$  is

$$N_{\gamma}(M_h) = N_{\text{ion}} \frac{M_h}{m_p}, \quad (6)$$

where  $N_{\text{ion}}$  is a dimensionless constant. We use the same  $N$ -body mass distribution and halo catalogues as that of the radiative transfer simulation described earlier. To simulate an ionization map at a specific redshift, we calculate the average ionizing photon number density  $\langle n_{\gamma}(\mathbf{x}) \rangle_R$  and H I atom number density  $\langle n_{\text{H}} \rangle_R$  within a spherical region of radius  $R$  around a point  $\mathbf{x}$  and compare them. This averaging and comparison is done for a range of smoothing scales, starting from the cell size ( $R_{\text{cell}}$ ) up to a certain maximum radius  $R_{\text{max}}$ , which is decided by the photon mean free path at that redshift. We consider the point  $\mathbf{x}$  to be ionized only if the condition

$$\langle n_{\gamma}(\mathbf{x}) \rangle_R \geq \langle n_{\text{H}} \rangle_R (1 + \bar{N}_{\text{rec}}) \quad (7)$$

(equation 7 of Choudhury et al. 2009) is satisfied for any smoothing radius  $R$ . The factor  $\bar{N}_{\text{rec}}$  is the average number of recombinations per hydrogen atom in the IGM. Note that various other unknown parameters e.g. the star-forming efficiency within the haloes, the number of photons per unit stellar mass, the photon escape fraction, the helium weight fraction, as well as the factor  $(1 + \bar{N}_{\text{rec}})$  are absorbed within the definition of  $N_{\text{ion}}$ . Given the mass and location of the haloes at a specific redshift, we tune the parameter  $N_{\text{ion}}$  to obtain a desired neutral fraction. Here, we do not consider a density-dependent recombination scenario and the effect of self-shielding, which can be added in these simulations (Choudhury et al. 2009). We set an ionization fraction equal to  $\langle n_{\gamma}(\mathbf{x}) \rangle_{R_{\text{cell}}} / \langle n_{\text{H}} \rangle_{R_{\text{cell}}}$  to the grid points where the above condition is not fulfilled. Finally, we tune the value of  $N_{\text{ion}}$  at each redshift to achieve a desired reionization history, i.e.  $x_{\text{HI}}$  versus  $z$ .

For our study, we consider an extreme reionization scenario which starts at  $z \sim 20$  and ends at  $z \sim 13.5$ . An LC slice through the 21-cm brightness temperature from the seminumerical simulation

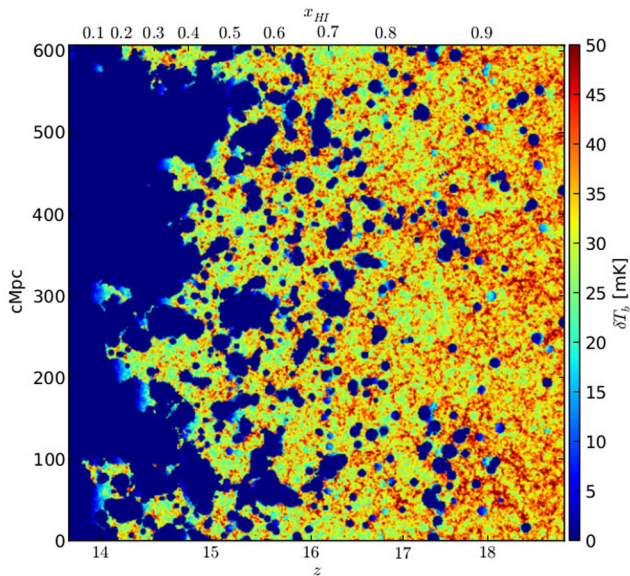


**Figure 2.** A slice through the 21-cm brightness temperature LC volume from the seminumerical simulation.

is shown in Fig. 2. In this scenario, 10 per cent, 50 per cent and 90 per cent (mass averaged) reionization occurs at redshifts 17.85, 15.2 and 14, respectively. The time period between 10 per cent and 90 per cent reionization is just  $\sim 88$  Myr – much faster than in our full numerical simulation for which the similar time-scale is  $\sim 400$  Myr. This rapid scenario is inconsistent with the latest results from the *WMAP* satellite (Hinshaw et al. 2013). However, it is illustrative of scenarios in which a few relatively bright sources drive reionization and has a reionization history which closely matches the ‘Pop III’ case in Barkana & Loeb (2006).

### 3 THE 21-CM POWER SPECTRUM AND ITS ANISOTROPIES

Although at large scales our Universe is isotropic, there are several effects that introduce differences between the H I 21-cm power spectrum  $P(k)$  measured along and perpendicular to the line of sight. To quantify this anisotropy in the power spectrum, the 21-cm power spectrum is often written as  $\Delta^2(k, \mu)$ , where  $\mu = k_{\parallel}/k$  and  $k_{\parallel}$  is the line-of-sight component of the Fourier mode  $k$ . The dimensionless power spectrum  $\Delta^2$  which is defined as  $\Delta^2 = k^3 P(k)/2\pi^2$  essentially measures the variance of fluctuations in the H I brightness maps at scales correspond to mode  $k$ . The parameter  $\mu$  which is also written as  $\cos \theta$  runs from  $-1$  to  $1$ ,  $\theta$  is the angle between the line of sight and the mode  $k$ .  $|\mu| = 1$  and  $0$  corresponds to the signal along and perpendicular to the line of sight, respectively. If the power spectrum is instead integrated over all  $\mu$  values, we refer to it as the spherically averaged H I 21-cm power spectrum,  $\Delta^2(k)$ .

One effect that makes the 21-cm power spectrum anisotropic is due to the gas peculiar velocities along the line of sight, which displace the 21-cm signal from its cosmological redshift. This is known as redshift space distortions and these carry unique information about the underlying matter density and the cosmic reionization (Barkana & Loeb 2005; Mao et al. 2012; Jensen et al. 2013; Majumdar, Bharadwaj & Choudhury 2013; Shapiro et al. 2013). The other effect is the Alcock–Paczynski effect which occurs when the use of inaccurate cosmological parameters introduce a mismatch in the calculation of physical scales along and perpendicular to the

line of sight (Alcock & Paczynski 1979; Ali, Bharadwaj & Pandey 2005; Nusser 2005; Barkana 2006).

In the linear regime, the anisotropic H I 21-cm power spectrum arising from the above two effects can be written as (Barkana 2006)

$$\Delta^2(k, \mu) = \Delta_0^2(k) + \Delta_{\mu^2}^2(k)\mu^2 + \Delta_{\mu^4}^2(k)\mu^4 + \Delta_{\mu^6}^2(k)\mu^6. \quad (8)$$

$\Delta_0^2(k)$  is the power spectrum that would be observed if there were no redshift space distortions and no Alcock–Paczynski effect in the signal.  $\Delta_{\mu^2}^2(k)$  is the cross-correlation power spectrum between the ionization and matter density fluctuations.  $\Delta_{\mu^4}^2(k)$  is the power spectrum of total matter density fluctuations multiplied by the mean H I brightness temperature squared. The Alcock–Paczynski effect introduces a  $\mu^6$  dependence in the power spectrum. The LC effect, being a line-of-sight effect, could in principle introduce additional anisotropies. In the subsequent sections, we study the anisotropies due to the LC effect. However, before we do so we first consider how the LC effect affects the spherically averaged H I 21-cm power spectrum.

## 4 RESULTS

### 4.1 Impact on the spherically averaged power spectrum

Fig. 3 shows the LC effect on the spherically averaged H I 21-cm power spectrum. We do not include  $k_{\perp} = 0$  modes throughout our work as this mode is not measurable by interferometric experiments. In this figure, we only present results from our numerical simulation. The redshift space distortion effect has not been included in this figure. The upper panel is for a sub-volume with line-of-sight extent  $\Delta L = 241$  Mpc from the full simulation box and the lower panel shows results for the full box of size 607 Mpc. The choice of  $\Delta L = 241$  Mpc allows us to probe the neutral fraction  $x_{\text{H I}}$  as low as 0.1. Smaller  $\Delta L$  will allow us to probe the LC effect for smaller  $x_{\text{H I}}$ . As we see later the LC effect is negligible for  $x_{\text{H I}} < 0.1$ , and so we do not consider sub-volumes of  $\Delta L < 241$  Mpc. The dashed and solid lines in the upper-left panel show the evolution of the spherically averaged power spectrum with and without the LC effect respectively as a function of the mass-averaged neutral fraction  $x_{\text{H I}}$  for different  $k$ -modes ( $k = 0.056, 0.15, 0.41, 1.03 \text{ Mpc}^{-1}$  from the top to bottom). Note that the power spectrum amplitudes for different  $k$ -modes are fixed arbitrarily to minimize overlap between the curves.

First considering the 241 Mpc results, we find that at large scales ( $k \lesssim 0.4 \text{ Mpc}^{-1}$ ) the power spectrum without the LC effect initially goes down when  $x_{\text{H I}}$  decreases from 1. There is a minimum in the power spectrum without the LC effect around  $x_{\text{H I}} \sim 0.8$ – $0.9$  for all  $k$ -modes we consider. During these early stages of reionization, mainly high-density peaks get ionized and therefore large-scale H I fluctuations are suppressed. This dip in the spherically averaged power spectrum has been seen in other works (Iliev et al. 2006; Jensen et al. 2013; Majumdar et al. 2013).

Beyond  $x_{\text{H I}} \sim 0.8$  the power at larger scales starts to grow rapidly as ionized bubbles grow substantially and provide fluctuations to the H I field at large scales. At the late stages of reionization, the power in the non-LC results again starts to drop due to a rapid decline in  $x_{\text{H I}}$ , and finally becomes zero at the end of the EoR. We find that the evolution in the spherically averaged power spectrum as a function of  $x_{\text{H I}}$  (or redshift) is most dramatic at large scales and is more gradual at smaller scales. For example, the spherically averaged power spectrum for  $k = 0.056 \text{ Mpc}^{-1}$  changes by around two orders of magnitude during the time period when  $x_{\text{H I}}$  changes

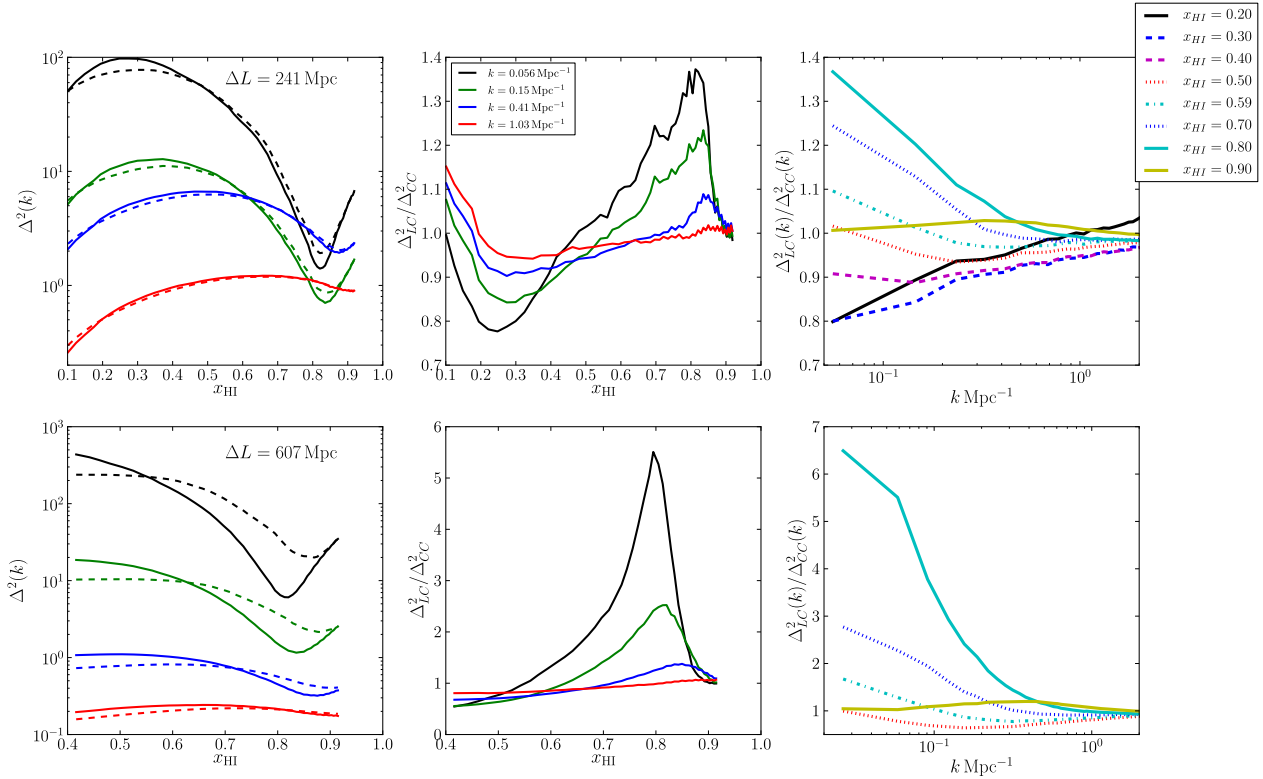


**Figure 3.** The LC effect on the spherically averaged power spectrum  $\Delta^2(k)$  of the H I 21-cm brightness temperature fluctuations. The upper panel considers a sub-volume of the line-of-sight extent  $\Delta L = 241$  Mpc from a full simulation box and the lower panel shows results for full box of size 607 Mpc. The solid and dashed lines in the upper-left panel represent the evolution of the spherically averaged power spectrum without and with the LC effect, respectively, as a function of the neutral fraction  $x_{\text{HI}}$  for different  $k$  values ( $k = 0.056, 0.15, 0.41, 1.03 \text{ Mpc}^{-1}$  from the top to bottom). Note that the power spectrum amplitudes for different  $k$ -modes are fixed arbitrarily for clarity in presentation. Here, the redshift space distortions have not been included. The middle and right-hand panels show the ratio between power spectra with and without the LC effect as function of the neutral fraction  $x_{\text{HI}}$  and  $k$ -mode, respectively.

from 0.8 to 0.2. At the smallest scale shown the changes are less than one order of magnitude.

The spherically averaged power spectrum with the LC effect included (dashed lines in the upper-left panel) is higher compared to the power spectrum without the LC effect during the initial stages ( $x_{\text{HI}} \sim 0.8$  to  $0.9$ ) and lower at the late stages of reionization for all  $k$ -modes we consider. This can be clearly seen in the upper-middle panel where we plot the ratio  $\frac{\Delta^2_{\text{LC}}(k)}{\Delta^2_{\text{CC}}(k)}$  between the spherically averaged power spectra with and without the LC effect. The ratio peaks around  $x_{\text{HI}} \sim 0.8$ – $0.9$  and dips around  $x_{\text{HI}} \sim 0.2$ – $0.3$ . For  $k = 0.056 \text{ Mpc}^{-1}$ , the ratio goes up to  $\sim 1.4$  at  $x_{\text{HI}} \sim 0.8$  and dips down to  $\sim 0.8$  at  $x_{\text{HI}} \sim 0.25$ . The ratio gradually approaches 1 at small scales. We note that during these two different stages of reionization, the evolution of the spherically averaged power spectrum without the LC effect is highly non-linear and rapid. Around  $x_{\text{HI}} \sim 0.8$  to  $0.9$ , there is a dip in the power spectrum and it grows rapidly on either side of this dip. The large-scale power spectrum peaks at around  $x_{\text{HI}} \sim 0.2$  to  $0.4$  and decreases rapidly on both sides of this peak.

This non-linear evolution of the power spectrum makes the LC effect very strong. On the other hand, the power spectrum around  $x_{\text{HI}} \sim 0.4$ – $0.5$  evolves more linearly with  $x_{\text{HI}}$  and hence the ratio is very close to 1, i.e. the LC effect is small. Therefore, we conclude that the LC effect for a given  $k$ -mode is mainly determined by the non-linear evolution of the power spectrum with the neutral fraction  $x_{\text{HI}}$ . This confirms our conclusion in Paper I – that the LC effect

will be determined by the terms  $\frac{d^{2n} \Delta^2(k, z)}{dr^{2n}}$ , where  $r$  is the comoving distance to redshift  $z$  and  $n \geq 1$ .

The upper-right panel of Fig. 3 shows the ratio between the spherically averaged power spectra with and without the LC effect as a function of  $k$ -mode for different neutral fractions  $x_{\text{HI}}$ . We find that initially when  $x_{\text{HI}} \gtrsim 0.9$  (solid yellow line) the ratio is close to 1, with slightly higher values at a scale of  $0.4 \text{ Mpc}^{-1}$ . We also find that the ratio gradually increases at larger scales during the first half and decreases in the second half of the EoR.

The bottom panels are the same as the upper panel except the line-of-sight length of the volume is  $\Delta L = 607 \text{ Mpc}$  in this case. Here, we cannot study the LC effect for the small neutral fraction  $x_{\text{HI}} < 0.4$  as LC volumes of line-of-sight width of  $\Delta L = 607 \text{ Mpc}$  centred around lower neutral fraction and redshift would extend beyond the redshift range of our simulations. The main difference between the 241 and 607 Mpc results is that in the latter the ratio between the spherically averaged power spectra with and without the LC effect is much higher but otherwise the results are qualitatively similar. For example for  $k \sim 0.056 \text{ Mpc}^{-1}$ , the ratio goes up to  $\sim 5.5$  around  $x_{\text{HI}} \sim 0.8$ . A larger impact of the LC effect is expected as the larger volume encompasses a much larger redshift range and therefore evolution of the 21-cm signal.

These results show that the power spectra of 21-cm data sets of very large frequency widths will be easier to measure, at least from the early stages of reionization, but also that we need to take the LC effect into account when analysing and interpreting such data sets.



We will discuss the optimum line-of-sight extent for analysing EoR H I 21-cm data in Section 7.

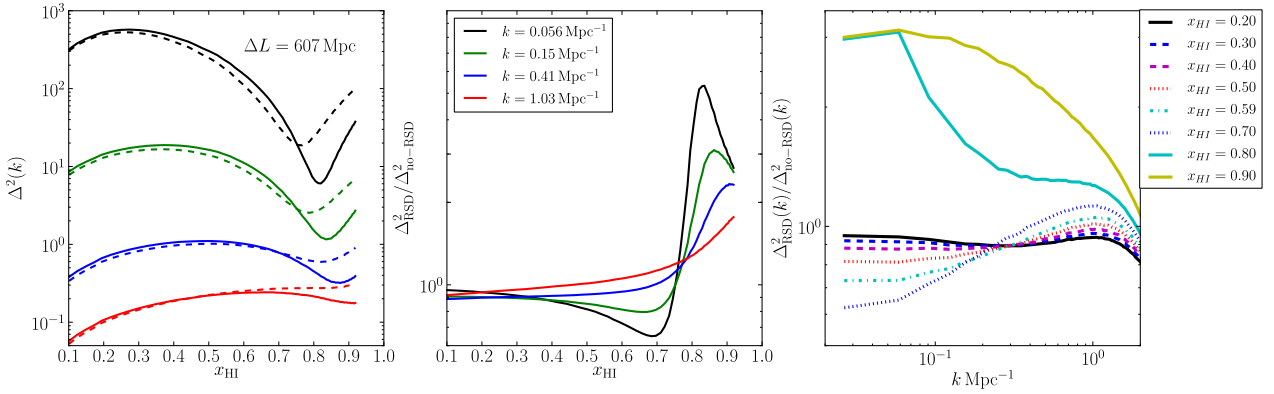
#### 4.2 Impact of redshift space distortions on the spherically averaged power spectrum

In order to compare the impact of the LC effect and the redshift space distortion effect, we start by presenting in Fig. 4 the spherically averaged H I 21-cm power spectrum in redshift space but without the LC effect. The  $k$ -modes are the same as in Fig. 3 and the line-of-sight extent of the underlying simulation is 607 Mpc. Interestingly, we find some similarities between the ways the redshift space distortions and the LC effect affect the spherically averaged H I 21-cm power spectrum. For both the power spectrum is affected more strongly at larger scales. The effect is most dramatic at the initial stages ( $x_{\text{HI}} \sim 0.8$ ) of the EoR, where the ratio between the spherically averaged H I 21-cm power spectra with and without the

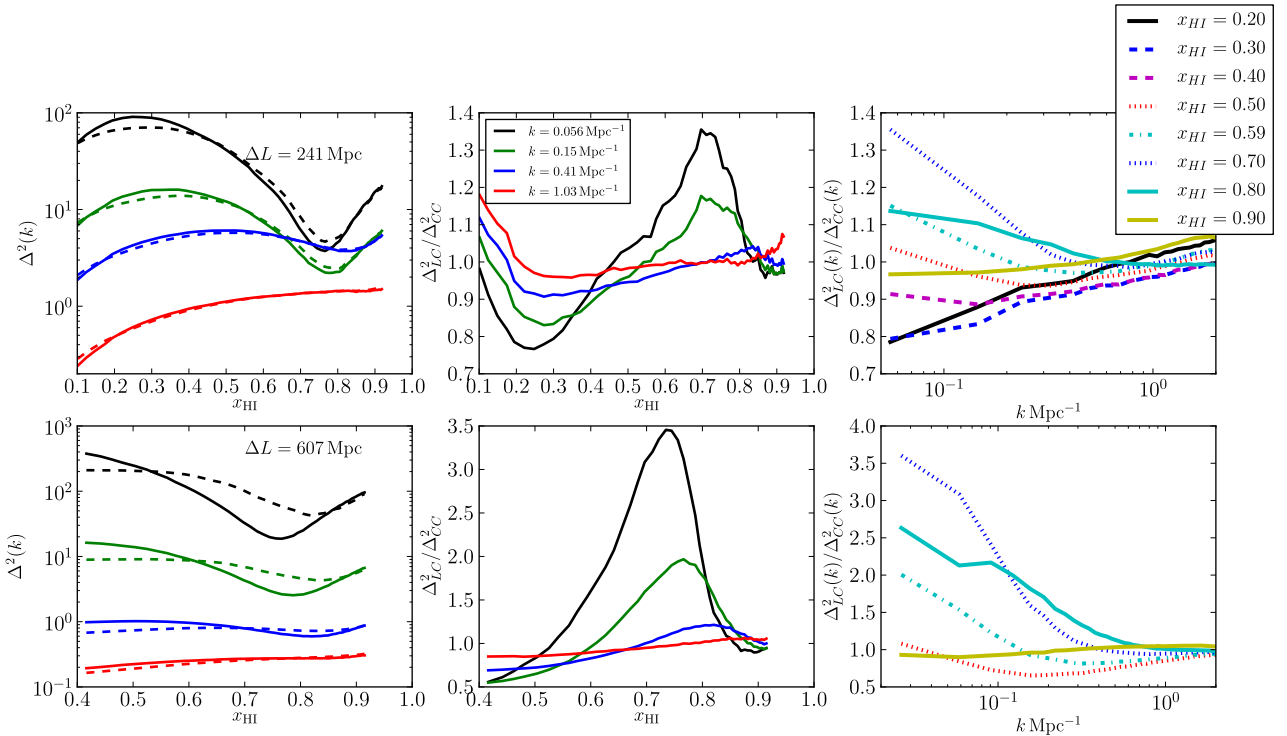
redshift space distortion effect reaches up to a factor of 6 for  $k = 0.056 \text{ Mpc}^{-1}$ . However, at small scales and during the later stages of the EoR this ratio comes close to 1. In contrast, the redshift space distortion effect is very small at the late stages of the EoR ( $x_{\text{HI}} \lesssim 0.3$ ), whereas the LC effect has a significant effect at both the early and late stages. The redshift space distortion effect does not depend on the line-of-sight length of the volume analysed, whereas the LC effect for obvious reasons does.

Fig. 5 shows the same results as Fig. 3 but including the redshift space distortion effect while calculating the spherically averaged power spectra with and without the LC effect. Although results are qualitatively same as in Fig. 3, we see that the peak in the ratio moves to lower  $x_{\text{HI}} \sim 0.7$  and the peak height is also lower compared to the case without redshift space distortions. We found similar results in our previous study (Paper I).

The enhancement of the spherically averaged power spectrum due to the LC effect around  $x_{\text{HI}} \sim 0.8\text{--}0.9$  is not seen in La Plante



**Figure 4.** Same as the lower panel of the Fig. 3, except here we include the redshift space distortion effect but not the LC effect. The solid and dashed lines in the left-hand panel correspond to the spherically averaged power spectrum without and with the redshift distortion effect, respectively.



**Figure 5.** Same as Fig. 3, but we include redshift space distortions while estimating power spectra with and without the LC effect.



et al. (2013). We find that this enhancement is due to the fact that the power spectrum without the LC effect becomes very small around that stage of reionization (see Figs. 3, 5) and therefore the ratio gets boosted. We believe that this dip in the power spectrum without the LC effect shows up due to the high-mass resolution of our simulations. We use  $5488^3$  DM particles, a total of  $10976^3$  cells in a comoving volume of  $(425/h \text{ Mpc})^3$ , whereas the above-mentioned work uses  $2048^3$  DM particles in a comoving volume of  $2/h$ , Gpc. This gives us  $\sim 2000$  times better particle mass resolution. Because of the coarser resolution in La Plante et al. (2013), the lower mass haloes which form early in the high-density peaks are not included and thus they will lack the early suppression of these high-density peaks.

### 4.3 Anisotropies in the power spectrum

We next consider the anisotropy in the observed H I 21-cm signal. Fig. 6 shows the H I 21-cm power spectrum  $\Delta^2(k, \mu)$  with the LC effect (upper panels) and the ratio between the power spectra with and without the LC effect (lower panels) as a function of  $\mu^2$  for different  $k$ -modes. As above we do not include  $k_\perp = 0$  modes here as these are unobservable with interferometers. Since we would like to investigate the anisotropy due to the LC effect only, we do not include the redshift space distortions here. Different lines in each panel represent different neutral fractions ranging from  $x_{\text{HI}} \sim 0.2$  to  $0.9$  for a fixed  $k$ -mode. The  $k$ -modes are  $0.056$ ,  $0.15$  and  $0.41 \text{ Mpc}^{-1}$  from the left- to right-hand panel, respectively. Note that the line-of-sight extents for different lines in each panel are different. When extracting sub-volumes with smaller line-of-sight extents than the full extent of the simulation, we always make sure that the mean neutral fraction  $x_{\text{HI}}$  for the coeval box and the central two-dimensional slice of the corresponding LC sub-volume are the same. The comoving distances from the centre to the two edges along the line of sight of the LC sub-volume are also kept

equal. The line-of-sight extent is the same for the coeval and LC sub-volumes for a fixed  $k$ -mode and neutral fraction  $x_{\text{HI}}$ . Since our focus is on the anisotropies, the amplitudes are not important here. We include  $1\sigma$  error bars due to sample variance. These have been calculated from  $\sqrt{2}\Delta^2(k, \mu)/\sqrt{N}$ , where  $N$  is the number of  $k$ -modes in the range  $k, k + dk$  and  $\mu, \mu + d\mu$ .

The black solid line shows results for the neutral fraction  $x_{\text{HI}} \sim 0.2$ . The non-smooth behaviour of the line arises because of the small number of available modes for it. The LC volume around  $x_{\text{HI}} \sim 0.2$  (redshift  $z = 6.94$ ) is only  $337 \text{ Mpc}$  wide along the line of sight (compared to  $607 \text{ Mpc}$  of full box) for the same reason as we used the  $241 \text{ Mpc}$  extent above in Section 4.1: reionization in our simulation finishes around redshift  $z = 6.48$ . Therefore, to have an LC box centred around redshift  $z = 6.94$  and one end at redshift  $z = 6.48$ , we can have a volume with at most  $337 \text{ Mpc}$  along the line of sight. The small number of  $k$ -modes increases the error bars for this line.

Inspection of the top row of Fig. 6 appears to reveal some variations of  $\Delta^2(k)$  with  $\mu$ , although comparison of different stages of reionization and  $k$ -modes does not suggest any systematic effects. In fact, when one compares these results to the ones without the LC effect it becomes apparent that the latter show similar features. In principle, the power spectra without the LC effect should not show any such  $\mu$ -dependence. This means that the apparent systematic change is not due to the LC effect but arises by chance. The way we calculate the error bars is valid if the underlying field is Gaussian. The reionization 21-cm signal is highly non-Gaussian, especially at late stages of the EoR, and therefore error bars may have been under-estimated.

This point is further illustrated by the lower panels of Fig. 6, where we plot the ratio between the power spectra with and without the LC effect. We observe that the ratio does not change significantly with  $\mu^2$ . We also do not observe any systematic changes with  $\mu^2$ . From all this we conclude that if the LC effect introduces any dependence

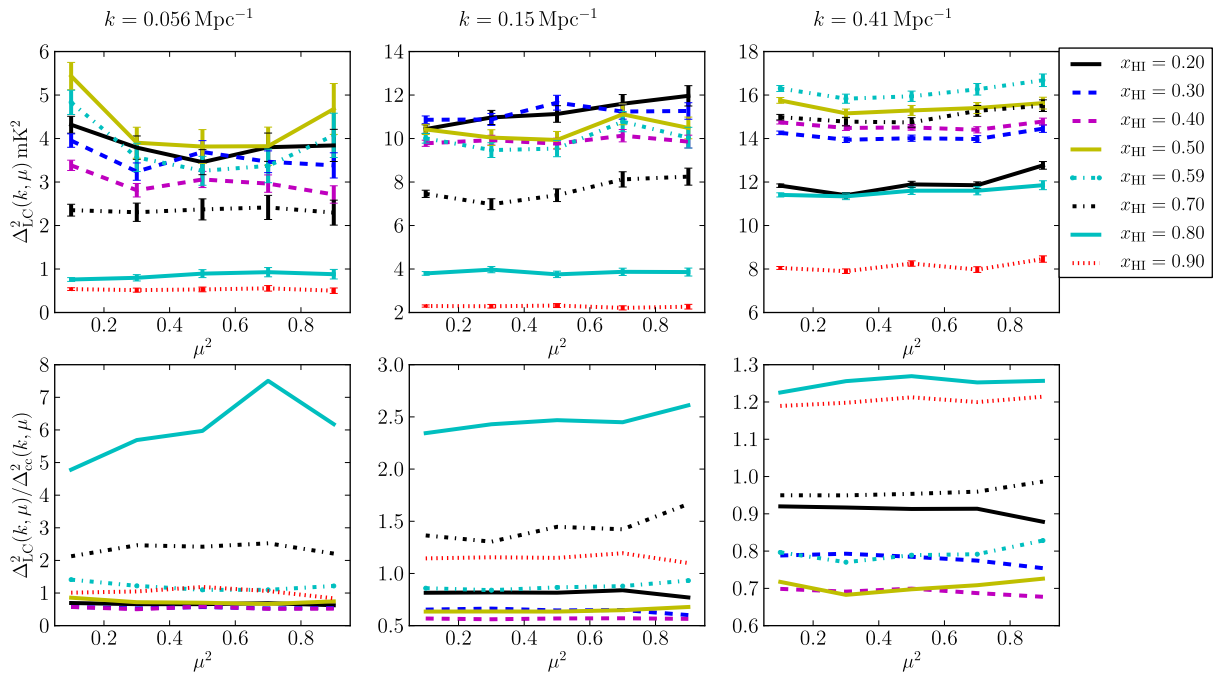


**Figure 6.** The power spectrum  $\Delta^2(k, \mu)$  (upper panels) with the LC effect and the ratio between power spectra with and without the LC effect (lower panels) as a function  $\mu^2$  for a given  $k$ -mode. Different lines in each panel represent different neutral fraction ranging from  $x_{\text{HI}} = 0.2$  to  $0.9$ . The  $k$ -mode is fixed for each panel.

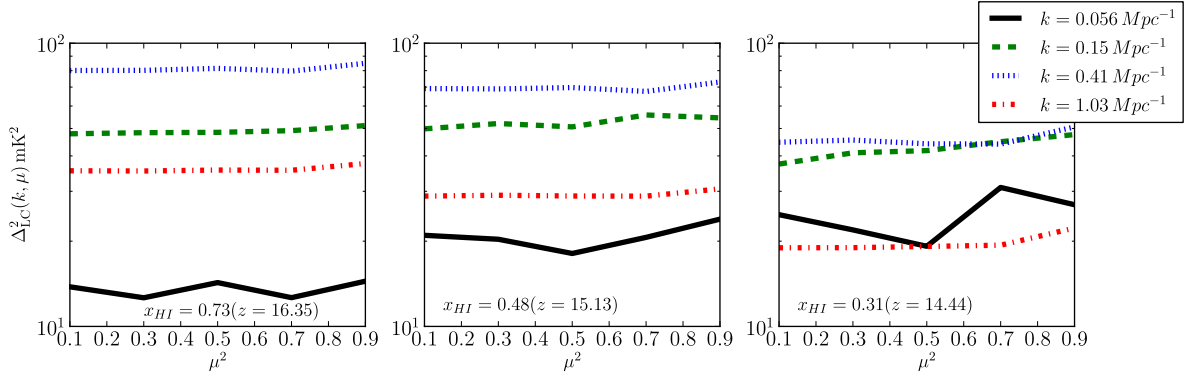


Figure 7. Power spectra as a function of  $\mu^2$  for different  $k$ -modes in the seminumerical simulations.

on  $\mu^2$  in the 21-cm power spectrum, it is so weak that it is buried in the sample variance.

To investigate whether a more rapid reionization scenario driven by fewer sources produces a stronger anisotropy (as claimed by Barkana & Loeb 2006), we show in Fig. 7 the anisotropy results for our seminumerical simulation. We show results around three central neutral fractions:  $x_{\text{HI}} = 0.77, 0.48$  and  $0.31$  (from the left-to right-hand panel). Even though reionization in the seminumerical simulation is  $\sim 4.5$  times faster than in numerical simulation and takes place much earlier (in the redshift range  $\sim 14$ – $19$ ), we still do not find any significant anisotropies in the H I 21-cm power spectra. We therefore conclude that the LC effect either does not make the EoR H I 21-cm power spectra anisotropic, i.e. a function of  $\mu^2$  or this dependence is so weak that it is buried in the sample variance. This is consistent with the recent work by La Plante et al. (2013) who also do not find any significant anisotropy due to the LC effect if  $k_{\perp} = 0$  modes are excluded.

We would like to reiterate here that the LC effect does have an overall effect on the power spectra as we observed in Fig. 3, i.e. the power spectrum is either enhanced or suppressed due to the effect but that enhancement/suppression is the same for all  $\mu$  for a given  $k$  and therefore does not introduce any observable  $\mu$ -dependence.

## 5 TOY MODELS

To better understand the lack of anisotropy due to the LC effect in the simulation results, we here use some simple toy models.

Let us consider  $N$  randomly placed spherical, non-overlapping ionized bubbles embedded in a uniform H I distribution in a cube. For simplicity, we assume that the signal from ionized and neutral regions are zero and one, respectively. The Fourier transform for a single spherical ionized bubble of radius  $R$  at position  $\mathbf{r}$  is

$$\delta(\mathbf{k}) = A(kR) \exp^{i\mathbf{k} \cdot \mathbf{r}}, \quad (9)$$

where  $A(kR) = 4/3\pi R^3 W(kR)$ . The spherical top-hat window function is defined as  $W(kR) = \frac{3}{k^3 R^3} (\sin(kR) - kR \cos(kR))$ . The Fourier transform for  $N$  randomly placed, non-overlapping, spherical bubbles of arbitrary sizes can be simply written as

$$\begin{aligned} \delta(\mathbf{k}) &= \sum_{j=1}^N A_j \exp^{i\mathbf{k} \cdot \mathbf{r}_j} \\ &= \sum_{j=1}^N A_j [\cos(\mathbf{k} \cdot \mathbf{r}_j) + i \sin(\mathbf{k} \cdot \mathbf{r}_j)], \end{aligned} \quad (10)$$

where  $A_j$  denotes  $A(kR_j)$ . The power spectrum  $P(\mathbf{k})$  for such a scenario can be written as

$$\begin{aligned} P(\mathbf{k}) &= \langle \delta(\mathbf{k}) \delta^*(\mathbf{k}) \rangle \\ &= \left\langle \left( \sum_{j=1}^N A_j \cos(\mathbf{k} \cdot \mathbf{r}_j) \right)^2 + \left( \sum_{j=1}^N A_j \sin(\mathbf{k} \cdot \mathbf{r}_j) \right)^2 \right\rangle \\ &= \sum_{j=1}^N A_j^2 + 2 \sum_{j=1, l=j+1}^{N-1, N} A_j A_l \cos(\mathbf{k} \cdot \Delta \mathbf{r}_{jl}), \end{aligned} \quad (11)$$

where  $\Delta \mathbf{r}_{jl} = \mathbf{r}_j - \mathbf{r}_l$ .

Now for the simplistic case, where all bubbles are same of radius  $R$ , the above equation reduces to

$$P(\mathbf{k}) = NA^2 + 2A^2 \sum_{j=1, l=j+1}^{N-1, N} \cos(\mathbf{k} \cdot \Delta \mathbf{r}_{jl}). \quad (12)$$

Since the bubbles are randomly placed, both  $\mathbf{r}_i$  and  $\mathbf{r}_j$  are random, therefore the difference vector  $\Delta \mathbf{r}_{jl}$  is random too. The phase term  $\mathbf{k} \cdot \Delta \mathbf{r}_{jl}$  can assume any value between  $-\pi$  to  $\pi$  (assuming that the  $\mathbf{r}_i$  vector is zero at the centre of the observed volume). This makes the second term in the above equation zero. Therefore, the above equation reduces to

$$P(\mathbf{k}) = NA^2. \quad (13)$$

Since  $A$  is only a function of  $|\mathbf{k}|$ , the power spectrum is isotropic, which is expected for the above case.

Now we consider a case where the bubble size changes systematically along the line of sight, but remains the same for a fixed line-of-sight location, i.e. a fixed redshift  $z$  (we refer to the right-hand panel of fig. 9 in Paper I). This is motivated by the fact that the inclusion of the LC effect makes the bubbles appear smaller/larger in the far/near side of an observed volume (see Fig. 1 in this paper or fig. 3 in Paper I). Note, however, that the individual bubbles are still spherical. In our simulations, we do not see any significant systematic elongation or compression in bubble shape due to the LC effect. This is expected as elongation or compression in bubble shapes occurs only when ionization fronts propagate relativistically (Yu 2005; Wyithe, Loeb & Barnes 2005; Shapiro et al. 2006; Sethi & Haiman 2008; Majumdar et al. 2011; Majumdar, Bharadwaj & Choudhury 2012).

We focus on bubbles only at two different line-of-sight locations, namely at  $r_{\parallel 1}$  and  $r_{\parallel 2}$ . In principle, there will be many bubbles at those two line-of-sight locations. Averaging over all those will make

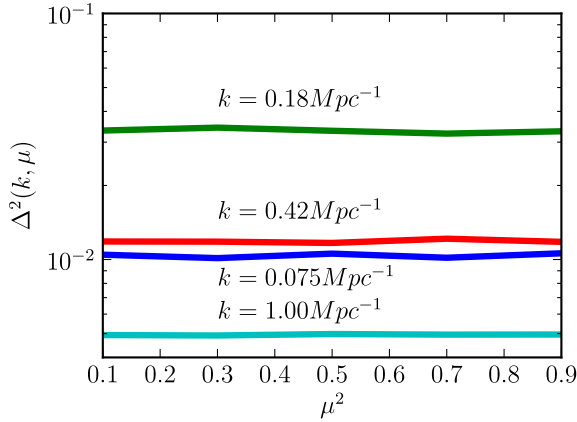


**Figure 8.** Power spectra as a function of  $\mu^2$  for different  $k$ -modes in the toy model described in Section 5.

the quantity  $A_j A_l \cos(\mathbf{k} \cdot \Delta \mathbf{r}_{jl})$  in equation (11) zero. Accordingly, all ‘cosine’ terms for all possible line-of-sight combinations will be zero and therefore the above equation can be reduced to

$$P(\mathbf{k}) = \sum_{j=1}^N A_j^2. \quad (14)$$

Like the previous case, the power spectrum here also is only dependent on  $|\mathbf{k}|$ , i.e. the power spectrum is isotropic.

We tested the above analytic result using simulations. In a simulation box, we put bubbles which are spherical, non-overlapping and randomly placed with a radius that changes with line-of-sight location. We assume that the bubble size changes linearly with line-of-sight location as  $R = R_0 + R_0(n_{\text{los}}/N - 1/2)$ , where  $N = 256$  is the total number of grid points along the line of sight and the line-of-sight index  $n_{\text{los}}$  varies from 0 to 255.  $R_0$  is assumed to be 10 Mpc, so the bubble size varies linearly with the los index from 5 Mpc in the far side to 15 Mpc in the front side. The box size is  $(256 \text{ Mpc})^3$ .

We simulate 500 independent realizations where the distribution of bubble centres changes in each simulation. Fig. 8 shows  $\Delta^2(k, \mu)$  as a function of  $\mu^2$  for different  $k$ -modes. It shows the ensemble average of all of the independent realizations. We find that the power spectrum is not changing with  $\mu^2$ , i.e. the power spectrum is isotropic and therefore supports our analytic predictions. We have also considered other models for the bubble size as a function of line-of-sight location, such as an exponential change where bubble size changes more drastically. We do not observe any anisotropy in any of those models. If the ionized bubbles were either prolate or oblate shaped of same size and oriented in the same direction, the power spectrum would become anisotropic as the Fourier transform of a prolate or an oblate spheroid is not spherically symmetric. However, as noted above, this is only true in the case of relativistically propagating ionization fronts.

Based on the above results, we conclude that the systematic change in the bubble size as a function of line of sight while individual bubble remains spherical is not enough to make the power spectrum anisotropic. Individual bubbles should be either systematically elongated or compressed to make the power spectrum anisotropic. In standard reionization by galaxies (like the ones we consider here), the ionized bubbles only appear to be smaller (in the far end) or larger (in near end) without any systematic elongation or compression. This explains the non-observance of significant anisotropy in the simulated power spectrum.

The above toy model considers only non-overlapping bubbles. Due to the clustering of ionizing sources, ionized bubbles overlaps with each other and therefore becomes highly non-spherical with some elongation or compression along the line of sight. Since the overlap of bubbles has no preferred direction, the signal will remain statistically isotropic. Therefore, our conclusions are also valid for the case where ionized bubbles overlap with each other.

## 6 THE TWO-POINT CORRELATION FUNCTION

Up to this point we have only considered the 21-cm power spectra in our analysis of the anisotropy due to the LC effect. However, a related but alternative quantity sometimes used for this is the two-point correlation function of the H I 21-cm brightness temperature fluctuations. Traditionally, the correlation function has been used to study the large-scale clustering of galaxies at lower redshifts (Peebles 1980; Davis & Peebles 1983; Landy & Szalay 1993). There has not been much attention on using the correlation function to quantify the EoR H I 21-cm signal, partly because the signal does not come from discrete sources but from the IGM. Another reason is that signal is observed in the Fourier domain and thus easy to analyse in the Fourier space.

Nevertheless, Furlanetto et al. (2004) developed analytic models to calculate the two-point correlation function for a given ionized bubble distribution. Ali et al. (2005) used it to study the impact of the Alock–Paczynski effect and the redshift space distortion effect on EoR H I 21-cm signal. Barkana & Loeb (2006) used it to first study the LC anisotropy in the EoR H I 21-cm signal. Recently Zawada et al. (2014) used numerical simulations and studied the same aspects of the EoR and pre-EoR H I 21-cm signal in more details. The two-point correlation function of the H I 21-cm brightness temperature is defined as

$$\xi(r, \mu_r, z) = \langle (\delta T_{b,1} - \bar{\delta T}_b(z_1)) \times (\delta T_{b,2} - \bar{\delta T}_b(z_2)) \rangle. \quad (15)$$

Note that  $\xi(r, \mu_r, z)$  is a function of the distance between two points  $r$  and redshifts  $z$ .  $\delta T_{b,i}$  is the H I 21-cm brightness temperature at position  $i$  corresponding to the redshift  $z_i$ . For the observed EoR H I signal, the correlation function, in principle, will also change with the angle  $\theta_r$  between the line-of-sight and the vector connecting the two points, where  $\mu_r = \cos \theta_r$ .  $z$  is the redshift at the mid-point connecting the two points.

Calculating the correlation function for the entire 3D simulation box for all possible correlation lengths and  $\mu_r$  is computationally expensive. The total number of operations to calculate the correlation function is  $\sim N^2/2$ , where  $N$  is the total number of grid cells in the simulation. Instead, we calculate the correlation function for fixed correlation lengths. In addition, we restrict the correlation to a plane parallel ( $\mu_r = 1$ ) and perpendicular ( $\mu_r = 0$ ) to the line of sight. Fig. 9 shows the two-point correlation function as a function of neutral fraction  $x_{\text{HI}}$  for a given correlation length  $r$  for the numerical simulation. Here, we only use our simulated LC volume to calculate the correlation functions. For  $\mu_r = 1$ , we correlate points taken from two different 2D slices perpendicular to the line of sight which are respectively  $r$  and  $r/2$  distance apart from each other and from the centre corresponding to neutral fraction  $x_{\text{HI}}$ . For  $\mu_r = 0$ , we correlate points taken from the central slice at neutral fraction  $x_{\text{HI}}$ . We see that due to the small number of pairs available, the correlation function is strongly affected by the sample variance. This restricts us from deriving robust conclusions about the LC effect on the correlation function.

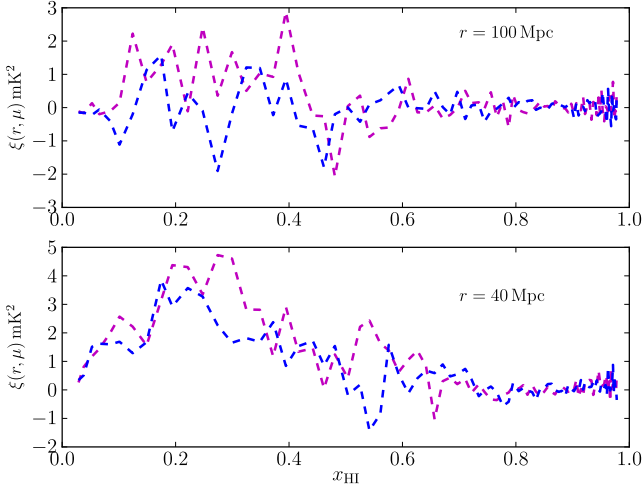
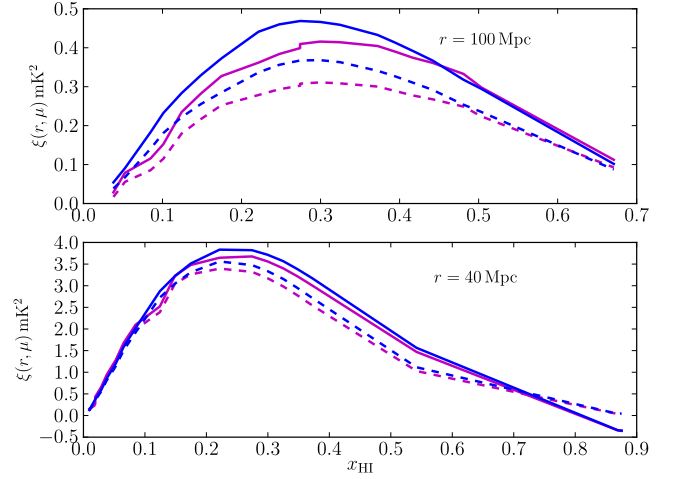


**Figure 9.** The two-point correlation function as a function of neutral fraction  $x_{\text{HI}}$  for a given correlation length  $r$  for the numerical simulation. We use the LC volume for this calculation. The magenta and blue lines show results for  $\mu_r = 1$  and  $\mu_r = 0$ , respectively. For  $\mu_r = 1$ , we correlate points taken from two different slices along the line of sight which are, respectively,  $r$  and  $r/2$  distance apart from each other and from the centre corresponding to neutral fraction  $x_{\text{HI}}$ . For  $\mu_r = 0$ , we correlate points taken from the 2D slice corresponding to neutral fraction  $x_{\text{HI}}$ .

To suppress the sample variance, we can construct multiple LCs from the simulation. Since we can pick any two-dimensional slice to correspond to a certain redshift, there are 504 different LCs that can be constructed from the simulations data. However, since we do not need the full LC for the correlation function analysis, we employ a short cut using the coeval volumes directly. To calculate the correlation function for the  $\mu_r = 1$  (line-of-sight) case and a specific correlation length  $r$ , we find pairs of coeval volumes ( $z_1, z_2$ ) whose difference in redshift ( $z_2 - z_1$ ) corresponds to  $r$ . We also find  $N_r$ , the number of cells that corresponds to a distance  $r$ . Next, we cross-correlate slice  $n$  from coeval volume  $z_1$  with slice  $N_r + n$  from coeval volume  $z_2$  for  $n$  running from 1 to 504,  $N = 504$  is the number of cells in one spatial direction in the coeval volumes. In this procedure, we use the periodic boundary conditions to handle the cases where  $N_r + n > N$ . For those cases, we use slice number  $N_r + n - N$ . With this procedure, we effectively use our complete data set to calculate the cross-correlations for  $\mu_r = 1$ , namely 504 slices of each  $(504)^2$  cells. This procedure is fully equivalent to constructing 504 LCs volumes without redshift space distortions and performing the correlation function analysis on these.

For the corresponding  $\mu_r = 0$  cross-correlations, we select a coeval volume corresponding to a redshift  $(z_1 + z_2)/2$  and then calculate the correlation function of that coeval volume.

For example, we have coeval 21-cm volumes at redshifts  $z = 7.059$  and  $7.348$  which are a comoving distance  $r \sim 100$  Mpc and  $N_r \approx 83$  grid cells apart. So we cross-correlate slice 1 from the simulation output at redshift  $z = 7.059$  with the 84th slice from the simulation output at redshift  $z = 7.348$ , and slice 2 with the 85th slice and so on. For this case, we use the coeval 21-cm volume at  $z = 7.221$  to calculate the  $\mu_r = 0$  cross-correlations. With this procedure, we effectively use our complete data set to calculate the cross-correlations for both values of  $\mu_r$ , namely 504 slices of each  $(504)^2$  cells. A larger number of measurements will suppress the sample variance considerably and we can study the correlation function at large length-scales, where the signal is weak.



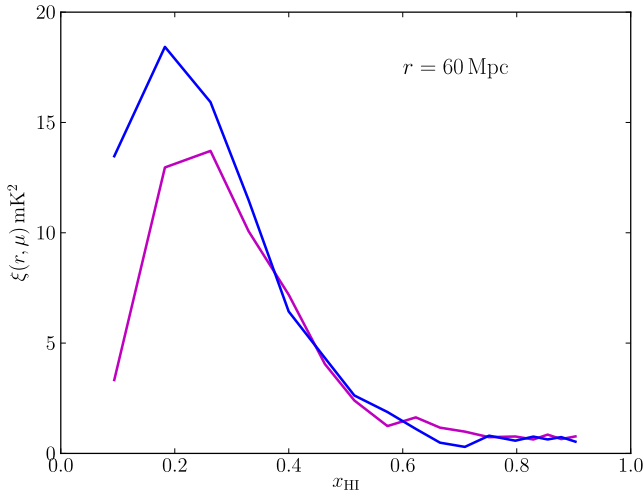
**Figure 10.** The two-point correlation function as a function of neutral fraction  $x_{\text{HI}}$  for a given correlation length  $r$  for the numerical simulation. Solid and dashed lines correspond to calculations with and without the redshift space distortion effect, respectively. The magenta and blue lines show results for  $\mu_r = 1$  and  $\mu_r = 0$ , respectively. Here, we have used the method described in Section 6 to perform the two-point correlation analysis on effectively 504 LC volumes thus suppressing the sample variance seen in Fig. 9.

Fig. 10 shows the correlation function as a function of neutral fraction  $x_{\text{HI}}$  for a given correlation length for the numerical simulation. Here, we see that the sample variance has been reduced considerably and we can study the LC effect on the correlation function. Dashed and solid lines correspond to without and with the redshift space distortion effect, respectively. The magenta and blue lines show results for  $\mu_r = 1$  and  $\mu_r = 0$ , respectively. We find that for the higher neutral fraction ( $x_{\text{HI}} \gtrsim 0.6$ ) the correlation function for  $\mu_r = 1$  (where the LC effect has been included) is the same as the corresponding  $\mu_r = 0$  lines even for a length-scale of  $r = 100$  Mpc.

As reionization progresses,  $\xi(r, \mu_r, z)$  for  $\mu_r = 1$  becomes lower than  $\mu_r = 0$ . They again match with each other at the end of reionization. This trend is found to be the same even if we include the redshift space distortion effect (solid lines). Both cases peak essentially at the same phase of reionization at  $x_{\text{HI}} \approx 0.28$  for  $r = 100$  Mpc and  $x_{\text{HI}} \approx 0.25$  for  $r = 40$  Mpc.

We find similar results for the seminumerical simulation which represents the case of an early and rapid reionization (Fig. 11). Unlike the numerical simulation, here the redshift space distortion effect hardly changes the results except at the beginning of the EoR and therefore we do not show them explicitly. In this case, the  $\mu_r = 1$  case appears to peak slightly earlier. When comparing these results to those in Barkana & Loeb (2006) and Zawada et al. (2014), several similarities and differences can be noted. As in Barkana & Loeb (2006), we find that the peak of  $\xi(\mu_r = 0)$  is the higher one. We also agree with those authors on the stage of reionization when the largest differences occur. However, in Barkana & Loeb (2006), the peaks are much more clearly separated (see their fig. 4), whereas we only find a small difference for the seminumerical simulation and none for the numerical one. Zawada et al. (2014) show that  $\xi(\mu_r = 1)$  peaks twice, once before and once after the peak in  $\xi(\mu_r = 0)$  (see their fig. 6). In contrast with both Barkana & Loeb (2006) and our results, the peaks are highest in the  $\xi(\mu_r = 1)$  case. All results agree that one needs to look at large scales ( $\sim 100$  Mpc)





**Figure 11.** The two-point correlation function as a function of neutral fraction  $x_{\text{HI}}$  for the seminumerical simulation without the redshift space distortion effect. The magenta and blue lines show results for  $\mu_r = 1$  and  $\mu_r = 0$ , respectively.

to see differences between the parallel and perpendicular correlation functions.

It is not obvious what causes these differences. Barkana & Loeb (2006) used very simplified analytic models. In the simulations of Zawada et al. (2014), low-mass haloes are missing. Very massive and luminous sources contribute to the reionization and hence the reionization history is very different from our simulations. Their results appear sample variance dominated, as the lines are not very smooth. This might explain the differences between our work and previous works. Another notable difference is that for our numerical result the signal strength is much smaller. For example, the peak values for  $\xi(r, \mu_r, z)$  are  $\sim 0.4 \text{ mK}^2$  and  $\sim 4 \text{ mK}^2$  for the correlation length  $r = 100$  and  $40 \text{ Mpc}$ . The above two papers find 5–10 times stronger signals. Small ionized regions and the resulting low variance of the 21-cm signal in our simulations compared to the other two could explain this.

The power spectrum and two-point correlation function contain the same basic information about the structure in the observed 21-cm brightness temperature field. So it must be true that they are either both isotropic or both anisotropic. However, the power spectra calculated for a fixed  $k$ -mode for different  $\mu_r$ -values (see Figs 6, 7) are similar. On the other hand the correlation function calculated for a fixed length-scale  $r$  for different  $\mu_r$ -values are found to be different.

The apparent inconsistency probably arises due to the way the correlation function is calculated. Like Barkana & Loeb (2006) and Zawada et al. (2014), we calculate the correlation function for  $\mu_r = 1$  (the plane that is parallel to the line of sight) by only considering those pairs whose middle point corresponds to a specific central redshift. For example, let us consider an LC volume which runs from  $z_{\text{start}}$  to  $z_{\text{end}}$ , corresponding to a comoving distance  $L_{\text{LC}}$ . If we want to measure the correlation function of this volume for a distance  $L$  ( $< L_{\text{LC}}$ ), we should find all pairs of slices along the line of sight which are a distance  $L$  apart. The value of this correlation function is the Fourier transform of the power spectrum measured at a scale  $k = 2\pi/L$ . However, this value is calculated from many different pairs of redshifts and mixes the signal from different phases of reionization. If we instead choose a specific pair of redshifts,  $z_1$  and  $z_2$  which are a distance  $L$  apart (with a central redshift  $z_c$ ), we

obtain a correlation function which does no longer correspond to the Fourier transform of the power spectrum measured at a scale  $k = 2\pi/L$  but which does measure the correlation at a specific phase of reionization. It is the latter quantity which we have studied in this section and appears to be more useful for picking out the anisotropy in LC data.

Finally, we note that the correlation function considered here is a measurable quantity. For a given redshift  $z_c$  and distance  $r$ , one picks images a distance  $r$  apart and straddling this redshift  $z_c$ . This way the correlation measurement belongs to a clear redshift, important for characterizing the LC effect. This method can be applied in a straightforward way to real data. However, as can be seen in Fig. 9 or in Zawada et al. (2014) for one field of view of several degrees across this measurement will be swamped by sample variance. Instruments like Low Frequency Array (LOFAR) and Square Kilometre Array (SKA) have fields of view of about  $\sim 5^\circ \times 5^\circ$ , comparable to the simulation size we consider here. The simulation results indicate that several hundreds of these would be needed to determine the cross-correlation with minimal sample variance. Given that these fields each need  $\sim 1000$  of hours of observation time, such numbers of fields will not be available. Thus, for LOFAR and SKA, this measurement is not actually feasible. However, experiments with larger field of view, such as Murchison Widefield Array (MWA) or Precision Array for Probing the Epoch of Reionization (PAPER), would only need tens of different patches which would allow a cross-correlation analysis, although it may be practically challenging.

## 7 OPTIMUM BANDWIDTH FOR ANALYSING OBSERVED DATA

When analysing the 21-cm power spectra above in Section 4.1, we consider two different values for the length of the line of sight (see Figs 3 and 5). We find that the LC effect on the H I 21-cm power spectrum is smaller for the shorter line of sight. It would be interesting to investigate how the LC effect changes as we change the length of our line of sight. Obviously, as we reduce the line of sight, the power spectra with and without the LC effect will start to converge.

In Fig. 12, we plot the ratio between the spherically averaged power spectra with and without the LC effect,  $\Delta_{\text{LC}}^2(k)/\Delta_{\text{CC}}^2(k)$ , as a function of the frequency bandwidth or equivalently the line-of-sight length for different  $k$ -modes and at different redshifts. The results are shown in redshift space, i.e. we incorporate the redshift space distortion effect in both the power spectra with and without the LC effect as it will be observed by an instrument.

In general, we find that the ratio deviates from 1 more for the higher bandwidth. For the neutral fraction  $x_{\text{HI}} = 0.3$  ( $z = 7.1$ ) (top-left panel), the ratio decreases with increasing value of the bandwidth. For example, for  $k = 0.056 \text{ Mpc}^{-1}$ , the ratio is about 0.55 at bandwidth = 27 MHz. The ratio gradually approaches 1 as we decrease the bandwidth. At 10 MHz, the ratio comes close to 0.9. We see similar trends for other  $k$ -modes. For  $x_{\text{HI}} = 0.5$  (top-right panel), the ratio for  $k = 0.056$  is very close to 1 even at larger bandwidth, consistent with our previous results. For  $k = 0.15$  and  $0.41 \text{ Mpc}^{-1}$ , the ratio departs considerably from 1 at the larger bandwidth. Around  $x_{\text{HI}} = 0.75$  (bottom-left panel), the ratio is always greater than 1 and very high for  $k = 0.056$  and  $0.15 \text{ Mpc}^{-1}$  consistent with our results (see Fig. 5). The ratio gradually decreases with bandwidth and converges to the value 1 as we decrease the bandwidth. In the early phases of the EoR, the LC effect is small and hence the ratio is always very close to 1 and the deviation is less than 10 per cent for all  $k$ -modes (see the bottom-right panel).

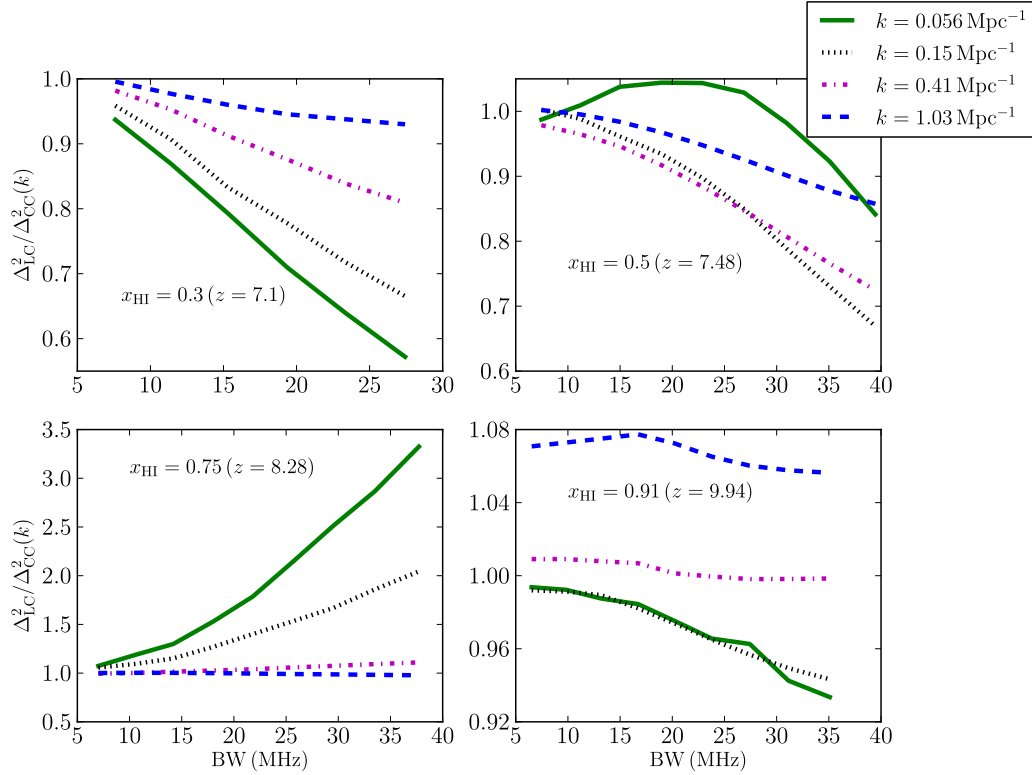


**Figure 12.** The ratio between power spectra with and without the LC effect as a function frequency bandwidth over which the power spectra have been evaluated. Note that the scale on the y-axis is different for the different panels.

It is now obvious that the LC effect should be considered if we estimate the EoR H I 21-cm power spectrum for longer line of sights, that is for very large frequency bandwidths, otherwise the predictions will be wrong or the data would be misinterpreted. Taking care of the LC effect properly may not be straightforward as the effect is highly model dependent. To avoid any complications that may arise due the uncertainty of modelling the LC effect, data analysis over smaller bandwidth is typically preferred (e.g. Harker et al. 2010). On the other hand, a large bandwidth is required to reduce the instrumental system noise and increase the sensitivity for detecting the signal. A larger bandwidth will also allow us to probe large line-of-sight scales, i.e. small  $k_{\parallel}$  (McQuinn et al. 2006).

Therefore, the optimum strategy would be to use a bandwidth as large as possible so that large-scale line-of-sight distances can be probed but still keeping the LC effect negligible. Therefore, prior knowledge about the optimum bandwidth would be useful for analysing the observed EoR H I 21-cm data, where the effect can be neglected. We now try to find this optimum bandwidth. In Fig. 13, we plot the bandwidth which allows a fractional change  $f$  in the power spectrum with the LC effect with respect to the power spectrum without the LC effect as a function of the neutral fraction  $x_{\text{HI}}$ . We define  $f$  as

$$f = \left| \frac{\Delta_{\text{LC}}^2(k)}{\Delta_{\text{CC}}^2(k)} - 1 \right|. \quad (16)$$

The upper panel shows results for  $f = 0.1$  for three different  $k$ -modes. This means that we calculate the bandwidth (or equivalently the line-of-sight width) for which the power spectrum with the LC effect deviates  $\leq 10$  per cent from the power spectrum without the effect. The gaps in the lines around  $x_{\text{HI}} \sim 0.5$  to  $0.7$  indicate that the optimum bandwidth for this neutral fraction range are much

higher than the extent of our full box size. We find that the optimum bandwidth changes with  $x_{\text{HI}}$  and the minimum optimum bandwidth for  $k = 0.056 \text{ Mpc}^{-1}$  is  $\sim 7.5$  MHz. For  $k = 0.15$  and  $0.41 \text{ Mpc}^{-1}$ , the optimum bandwidth is  $\sim 11$  and  $\sim 16$  MHz, respectively.

If we allow the fractional change to be  $f = 0.2$  (see lower panel), the optimum bandwidth becomes higher:  $\sim 11$ ,  $\sim 16$  and  $27$  MHz for  $k = 0.056$ ,  $0.15$  and  $0.41 \text{ Mpc}^{-1}$ , respectively. Our results suggest that if one wants to analyse the power spectrum at modes  $k \gtrsim 0.056 \text{ Mpc}^{-1}$  and one is ready to neglect 10 per cent error in the power spectrum, the data should be analysed over the bandwidth  $\lesssim 7.5$  MHz. For higher  $k$ -modes and larger fractional change  $f$ , a larger optimum bandwidth is allowed. The above estimate will change for different reionization models. Since in our numerical simulation the reionization is more gradual and extended, the LC effect is smaller, and therefore our estimate gives a rough idea about the optimum bandwidth and should be considered as an upper limit.

## 8 SUMMARY AND DISCUSSION

We use the largest size (607 Mpc) radiative transfer simulation of the EoR to date to investigate the impact of the LC effect on the EoR H I 21-cm signal. In particular, we focus on the evolution of the effect at different scales during the EoR, anisotropies in the H I 21-cm signal and observational implications. We present results both in real and redshift space by including the effects of peculiar velocities.

We find that the LC effect is most dramatic at two different stages of the EoR: one when reionization is  $\sim 20$  per cent and other when it is  $\sim 80$  per cent finished. The effect is relatively small at  $\sim 50$  per cent reionization, consistent with our previous results. We argue that the non-linear evolution of the power spectrum as a function of

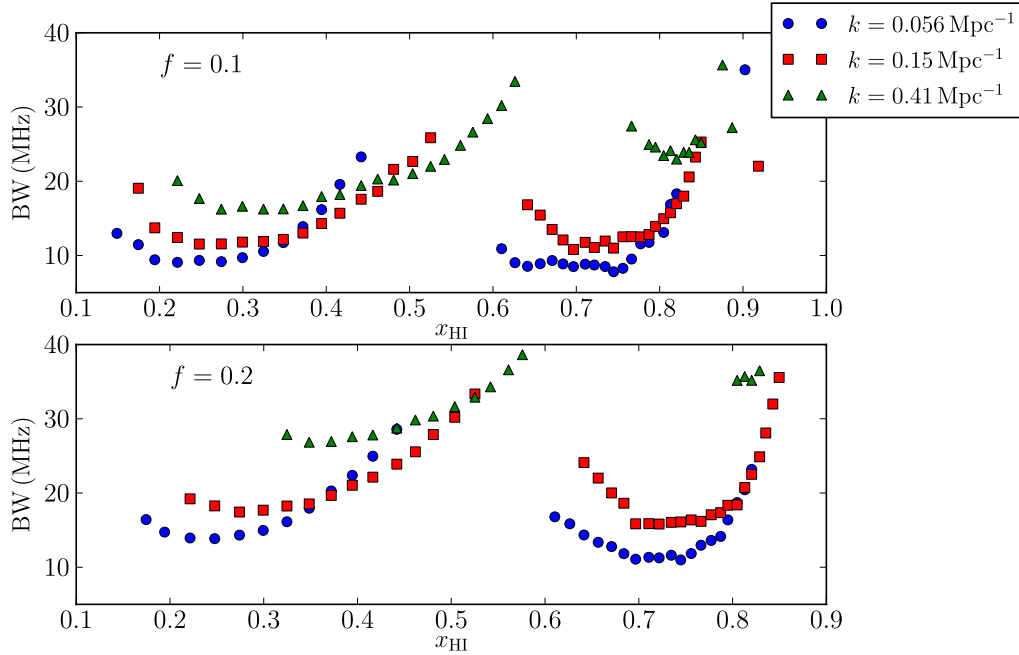


**Figure 13.** The optimum bandwidth for analysing observed EoR H I 21-cm data as a function of the neutral fraction  $x_{\text{HI}}$  for different  $k$ -modes. The gap in each line around  $x_{\text{HI}} \sim 0.5$  to  $0.7$  indicates that the optimum bandwidth for those neutral fractions are much higher than full box size.

comoving distance from the present determines the LC effect where any linear evolution gets averaged out. We observe up to  $\sim 40$  per cent and  $\sim 25$  per cent change at the largest scale available for a line-of-sight length of 241 Mpc. When we use the entire simulation box (607 Mpc), we find a factor of  $\sim 4$  amplification in the power spectrum at  $x_{\text{HI}} \sim 0.75$ .

We find some similarities between the ways the LC and the redshift space distortion effect affect the spherically averaged H I 21-cm power spectrum. For example, both effects enhance the power spectra significantly at large scales and at the initial stages ( $x_{\text{HI}} \sim 0.8$ ) of the EoR. However, the redshift space distortion effect becomes very small at the late stages of the EoR ( $x_{\text{HI}} \lesssim 0.3$ ) unlike the LC effect which also has a significant effect at the late stages. Unlike the redshift space distortion effect, the LC effect depends on the length of the line of sight used in the analysis.

Somewhat surprisingly, we do not observe any significant anisotropy in the H I 21-cm power spectrum due to the LC effect. We find similar results in our seminumerical simulation of an early rapid reionization. The models used in this paper did not result in relativistically propagating ionization fronts and therefore the ionized bubbles do not get elongated or compressed systematically due to the LC effect. They only appear smaller or bigger without changing the shape drastically. Using relevant toy models, we argue that the systematic change in the bubble sizes as a function of the line-of-sight position while individual bubbles remain spherical is not enough to make the power spectrum anisotropic. Individual bubbles should be either elongated or compressed to make the power spectrum anisotropic. The reason that ionized bubbles in our simulations do not get elongated or compressed is that sources are not bright enough to make the ionization front relativistic which is an important property to make bubbles elongated or compressed.

We also calculate the two-point correlation function of the H I 21-cm brightness temperature fluctuations. The two-point correlation function for a given length-scale peaks around  $x_{\text{HI}} \sim 0.3$ . When we calculate the correlation functions along and perpendicular to

the line of sight, they are found to be different for the scales of  $\sim 100$  Mpc and late stages of reionization. This is consistent with earlier works. This apparent ‘anisotropy’ found in the correlation function is due to the differences in the way we calculate the two correlation functions along and perpendicular to the line of sight. We consider all possible correlations when we calculate it for perpendicular to the line of sight, whereas we impose some restrictions while calculating it along the line of sight. However, for small scales ( $\lesssim 40$  Mpc) and in the early stages, the parallel and perpendicular correlation functions are identical.

The LC effect is obviously dependent on the line-of-sight extent over which the signal is being analysed. The smaller the line-of-sight extent or frequency bandwidth, the smaller the effect. We go on to calculate the ‘optimum bandwidth’ for predicting or analysing EoR H I 21-cm power spectra. The optimum bandwidth is the highest bandwidth allowed for analysing the EoR H I 21-cm power spectra for which the LC effect can be neglected. We find that the optimum bandwidth for  $k = 0.056 \text{ Mpc}^{-1}$  is  $\sim 7.5$  MHz. For  $k = 0.15$  and  $0.41 \text{ Mpc}^{-1}$ , the optimum bandwidth is  $\sim 11$  and  $\sim 16$  MHz, respectively, if we can neglect a 10 per cent change in the power spectra.

These results might change for different reionization models. Our reionization model is extended (extended over  $\Delta z \approx 3$ ) and sources are relatively weak. Therefore, we think that the LC effect presented here is on the lower side. Therefore, the optimum bandwidth would be smaller for more rapid reionization models. However, we believe that our results provide a reasonable estimate of the effect. The signal is also expected to be isotropic or weakly anisotropic, unless reionization is dominated by very bright sources like supermassive quasars. The relatively high value of the electron scattering optical depth combined with the measurements of the UV background around  $z \sim 6$  do suggest a more extended reionization.

It has been proposed that the EoR H I 21-cm signal can be used to extract the ‘pure’ dark matter power spectrum through a fitting of the anisotropic power spectrum (Barkana & Loeb 2006; Shapiro

et al. 2013). In addition, the signal contains information about the correlation between the distribution of the sources of radiation and the matter density and can thus be used to characterize the sources of reionization (Jensen et al. 2013). The impact of the LC effect on the above issues has not been investigated in details although Jensen et al. (2013) included the effect. Our results show that the LC effect does not introduce any anisotropy in the power spectrum, which suggests that ignoring the LC effect in such studies is probably valid.

In this paper, we only considered the high spin temperature case for which the HI 21-cm signal appears in emission. However, during the pre-reionization phase, spin temperature variations may cause the signal to appear in absorption and results may differ from what we find here (Zawada et al. 2014). We would like to investigate this in more detail in future.

## ACKNOWLEDGEMENTS

KKD thanks the Department of Science and Technology (DST), India for the research grant SR/FTP/PS-119/2012 under the Fast Track Scheme for Young Scientist. KKD is grateful for financial support from Swedish Research Council (VR) through the Oscar Klein Centre (grant 2007-8709). KKD would like to thank Tirthankar Roy Choudhury and Raghunath Ghara for useful discussion. GM is supported by Swedish Research Council grant 2012-4144. YM was supported by French state funds managed by the ANR within the Investissements d’Avenir programme under reference ANR-11-IDEX-0004-02. PRS was supported in part by US NSF grants AST-0708176 and AST-1009799, and NASA grants NNX07AH09G and NNX11AE09G. KA was supported in part by NRF grant funded by the Korean government MEST (No. 2012R1A1A1014646). This work was supported by the Science and Technology Facilities Council [grant numbers ST/F002858/1 and ST/I000976/1]; and The Southeast Physics Network (SEPNet). The authors acknowledge the US NSF TeraGrid/XSEDE Project AST090005 and the Texas Advanced Computing Center (TACC) at The University of Texas at Austin for providing HPC resources that have contributed to the research results reported within this paper. This research was supported in part by an allocation of advanced computing resources provided by the National Science Foundation through TACC and the National Institute for Computational Sciences (NICS), with part of the computations performed on Lonestar at TACC (<http://www.tacc.utexas.edu>) and Kraken at NICS (<http://www.nics.tennessee.edu>). Some of the numerical computations were done on the Apollo cluster at The University of Sussex and the Sciama High Performance Compute (HPC) cluster which is supported by the ICG, SEPNet and the University of Portsmouth. Part of the computations were performed on the GPC supercomputer at the SciNet HPC Consortium. SciNet is funded by the Canada Foundation for Innovation under the auspices of Compute Canada, the Government of Ontario, Ontario Research Fund - Research Excellence and the University of Toronto.

## REFERENCES

Alcock C., Paczynski B., 1979, *Nature*, 281, 358  
 Ali S. S., Bharadwaj S., Pandey B., 2005, *MNRAS*, 363, 251  
 Ali S. S., Bharadwaj S., Chengalur J. N., 2008, *MNRAS*, 385, 2166  
 Baek S., Di Matteo P., Semelin B., Combes F., Revaz Y., 2009, *A&A*, 495, 389  
 Barkana R., 2006, *MNRAS*, 372, 259  
 Barkana R., Loeb A., 2005, *ApJ*, 624, L65

Barkana R., Loeb A., 2006, *MNRAS*, 372, L43  
 Battaglia N., Trac H., Cen R., Loeb A., 2013, *ApJ*, 776, 81  
 Bernardi G. et al., 2009, *A&A*, 500, 965  
 Bernardi G. et al., 2013, *ApJ*, 771, 105  
 Bharadwaj S., Ali S. S., 2005, *MNRAS*, 356, 1519  
 Bittner J. M., Loeb A., 2011, *J. Cosmol. Astropart. Phys.*, 4, 38  
 Bowman J. D., Rogers A. E. E., 2010, *Nature*, 468, 796  
 Chapman E. et al., 2013, *MNRAS*, 429, 165  
 Choudhury T. R., Haehnelt M. G., Regan J., 2009, *MNRAS*, 394, 960  
 Datta K. K., Bharadwaj S., Choudhury T. R., 2007, *MNRAS*, 382, 809  
 Datta K. K., Friedrich M. M., Mellema G., Iliev I. T., Shapiro P. R., 2012a, *MNRAS*, 424, 762  
 Datta K. K., Mellema G., Mao Y., Iliev I. T., Shapiro P. R., Ahn K., 2012b, *MNRAS*, 424, 1877 (Paper I)  
 Davis M., Peebles P. J. E., 1983, *ApJ*, 267, 465  
 Furlanetto S. R., Zaldarriaga M., Hernquist L., 2004, *ApJ*, 613, 1  
 Geil P. M., Wyithe J. S. B., 2008, *MNRAS*, 386, 1683  
 Ghosh A., Prasad J., Bharadwaj S., Ali S. S., Chengalur J. N., 2012, *MNRAS*, 426, 3295  
 Harker G. J. A. et al., 2009, *MNRAS*, 393, 1449  
 Harker G. et al., 2010, *MNRAS*, 405, 2492  
 Harnois-Déraps J., Pen U.-L., Iliev I. T., Merz H., Emberson J. D., Desjacques V., 2013, *MNRAS*, 436, 540  
 Hinshaw G. et al., 2013, *ApJS*, 208, 19  
 Iliev I. T. et al., 2006, *MNRAS*, 371, 1057  
 Iliev I. T., Mellema G., Shapiro P. R., Pen U.-L., 2007, *MNRAS*, 376, 534  
 Iliev I. T., Mellema G., Ahn K., Shapiro P. R., Mao Y., Pen U.-L., 2014, *MNRAS*, 439, 725  
 Jacobs D. C. et al., 2013, *ApJ*, 776, 108  
 Jelić V. et al., 2008, *MNRAS*, 389, 1319  
 Jensen H. et al., 2013, *MNRAS*, 435, 460  
 La Plante P., Battaglia N., Natarajan A., Peterson J. B., Trac H., Cen R., Loeb A., 2013, preprint (arXiv:1309.7056)  
 Landy S. D., Szalay A. S., 1993, *ApJ*, 412, 64  
 Majumdar S., Bharadwaj S., Datta K. K., Choudhury T. R., 2011, *MNRAS*, 413, 1409  
 Majumdar S., Bharadwaj S., Choudhury T. R., 2012, *MNRAS*, 426, 3178  
 Majumdar S., Bharadwaj S., Choudhury T. R., 2013, *MNRAS*, 434, 1978  
 Majumdar S., Mellema G., Datta K. K., Jensen H., Choudhury T. R., Bharadwaj S., Friedrich M. M., 2014, preprint (arXiv:1403.0941)  
 Malloy M., Lidz A., 2013, *ApJ*, 767, 68  
 Mao Y., Shapiro P. R., Mellema G., Iliev I. T., Koda J., Ahn K., 2012, *MNRAS*, 422, 926  
 Maselli A., Gallerani S., Ferrara A., Choudhury T. R., 2007, *MNRAS*, 376, L34  
 McQuinn M., Zahn O., Zaldarriaga M., Hernquist L., Furlanetto S. R., 2006, *ApJ*, 653, 815  
 McQuinn M., Lidz A., Zahn O., Dutta S., Hernquist L., Zaldarriaga M., 2007, *MNRAS*, 377, 1043  
 Mellema G., Iliev I. T., Alvarez M. A., Shapiro P. R., 2006a, *New Astron.*, 11, 374  
 Mellema G., Iliev I. T., Pen U.-L., Shapiro P. R., 2006b, *MNRAS*, 372, 679  
 Mellema G. et al., 2013, *Exp. Astron.*, 36, 235  
 Merz H., Pen U.-L., Trac H., 2005, *New Astron.*, 10, 393  
 Mesinger A., Furlanetto S., 2007, *ApJ*, 669, 663  
 Morales M. F., Hewitt J., 2004, *ApJ*, 615, 7  
 Morales M. F., Wyithe J. S. B., 2010, *ARA&A*, 48, 127  
 Nusser A., 2005, *MNRAS*, 364, 743  
 Paciga G. et al., 2013, *MNRAS*, 433, 639  
 Parsons A. R. et al., 2010, *AJ*, 139, 1468  
 Parsons A. R. et al., 2013, preprint (arXiv:1304.4991)  
 Patil A. H. et al., 2014, preprint (arXiv:1401.4172)  
 Peebles P. J. E., 1980, *The Large-Scale Structure of The Universe*. Princeton Univ. Press, Princeton, NJ, p. 435  
 Pen U.-L., Chang T.-C., Peterson J. B., Roy J., Gupta Y., Bandura K., 2008, in Minchin R., Momjian E., eds, *AIP Conf. Ser.*, Vol. 1035, *The Evolution of Galaxies Through the Neutral Hydrogen Window*. Am. Inst. Phys., New York, p. 75



- Pen U.-L., Chang T.-C., Hirata C. M., Peterson J. B., Roy J., Gupta Y., Odegova J., Sigurdson K., 2009, MNRAS, 399, 181
- Planck Collaboration et al., 2013, A&A, preprint ([arXiv:1303.5076](https://arxiv.org/abs/1303.5076))
- Pritchard J. R., Loeb A., 2012, Rep. Prog. Phys., 75, 086901
- Santos M. G., Amblard A., Pritchard J., Trac H., Cen R., Cooray A., 2008, ApJ, 689, 1
- Sethi S., Haiman Z., 2008, ApJ, 673, 1
- Shapiro P. R., Iliev I. T., Alvarez M. A., Scannapieco E., 2006, ApJ, 648, 922
- Shapiro P. R., Mao Y., Iliev I. T., Mellema G., Datta K. K., Ahn K., Koda J., 2013, Phys. Rev. Lett., 110, 151301
- Shin M.-S., Trac H., Cen R., 2008, ApJ, 681, 756
- Thomas R. M. et al., 2009, MNRAS, 393, 32
- Tingay S. J. et al., 2013, Publ. Astron. Soc. Aust., 30, 7
- van Haarlem M. P. et al., 2013, A&A, 556, A2
- Wyithe J. S. B., Loeb A., Barnes D. G., 2005, ApJ, 634, 715
- Yatawatta S. et al., 2013, A&A, 550, A136
- Yu Q., 2005, ApJ, 623, 683
- Zahn O., Lidz A., McQuinn M., Dutta S., Hernquist L., Zaldarriaga M., Furlanetto S. R., 2007, ApJ, 654, 12
- Zaldarriaga M., Furlanetto S. R., Hernquist L., 2004, ApJ, 608, 622
- Zaroubi S. et al., 2012, MNRAS, 425, 2964
- Zawada K., Semelin B., Vonlanthen P., Baek S., Revaz Y., 2014, MNRAS, 439, 1615

This paper has been typeset from a  $\text{\LaTeX}$  file prepared by the author.